Electron temperature gradient driven transport model for tokamak plasmas

View Online   Export Citation   CrossMark

T. Rafiq,[1,a)] ⓘD C. Wilson,[1] ⓘD L. Luo,[1] J. Weiland,[1] E. Schuster,[1] A. Y. Pankin,[2] ⓘD W. Guttenfelder,[2] ⓘD and S. Kaye[2] ⓘD

AFFILIATIONS

[1]Lehigh University, Bethlehem, Pennsylvania 18015-3085, USA
[2]Princeton Plasma Physics Laboratory, Princeton, New Jersey 08543, USA

a)Author to whom correspondence should be addressed: rafiq@lehigh.edu

ABSTRACT

A new model for electron temperature gradient (ETG) modes is developed as a component of the multi-mode anomalous transport module [Rafiq *et al.*, Phys Plasmas **20**, 032506 (2013)] to predict a time-dependent electron temperature profile in conventional and low aspect ratio tokamaks. This model is based on two-fluid equations that govern the dynamics of low-frequency short- and long-wavelength electromagnetic toroidal ETG driven drift modes. A low collisionality NSTX discharge is used to scan the plasma parameter dependence on the ETG real frequency, growth rate, and electron thermal diffusivity. Electron thermal transport is discovered in the deep core region where modes are more electromagnetic in nature. Several previously reported gyrokinetic trends are reproduced, including the dependencies of density gradients, magnetic shear, β and gradient of β (β'), collisionality, safety factor, and toroidicity, where β is the ratio of the plasma pressure to the magnetic pressure. The electron heat diffusivity associated with the ETG mode is discovered to be on a scale consistent with the experimental diffusivity determined by power balance analysis.

I. INTRODUCTION

Ion temperature gradient (ITG) modes, which mainly contribute to ion thermal transport in conventional tokamaks (higher aspect ratio), are often stable in low aspect ratio NSTX neutral beam injected heated discharges.[1] This is due to the combined effects of plasma β, gradient of plasma β (β'), Shafranov shift, geometry, and large $\mathbf{E} \times \mathbf{B}$ flow shear, where plasma β is the ratio of the plasma pressure to the magnetic pressure. As a result of these combined effects, low aspect ratio tokamaks operate in a regime where the electron thermal transport dominates the ion thermal transport. One of the modes that is responsible for the electron thermal transport is the electron temperature gradient (ETG) mode.[2–18] ETG modes have a wavelength that is much larger than the electron gyroradius but much smaller than the ion gyroradius, indicating that they are of the short wavelength nature. ETG modes exist in both slab and toroidal versions and can be unstable in both conventional and low-aspect ratio tokamaks and propagate in the direction of the electron drift frequency. ETG modes can have a large poloidal wavenumber (k_θ)[19] but a small radial wavenumber (k_r), resulting in radially elongated structures known as streamers[20] that can drive significantly more electron thermal transport than ITG modes. Here, $k_\theta(k_r)$ is the wavenumber perpendicular to both the magnetic field and the radial (poloidal) direction.

Burning plasma discharges in which collisions with fast alpha particles primarily heat electrons, Ohmic heated plasmas, plasmas with an internal transport barrier (ITB),[21] and plasmas with electron cyclotron heating all benefit from a better understanding of ETG turbulence and transport. The transition of tokamak discharge from L- to I-mode, which is a reduced transport regime between L- and H-mode, is also better understood in terms of transport associated with ETG modes.[22] This insight into electron thermal transport due to ETG modes will aid in the prediction and optimization of transport in present and future experiments, such as ITER and the Fusion Pilot Plant. It has been found that as collisionality changes, the toroidal rotation profile changes, and the resulting flow shear can provide an effective suppression mechanism for ETG turbulence at marginal stability in NSTX discharges.[23] Furthermore, a reverse magnetic shear and a high density gradient can inhibit the electron thermal transport.[24] Unfortunately, the current ETG model available in the multi-mode anomalous transport module (MMM)[25] does not account for collisionality, plasma beta, gradient of beta, drift resonances, drift reversal, reverse magnetic shear, or flow-shear effects. The absence of these effects explains why MMM simulations of the NSTX electron temperature profile do not reproduce some experimental trends.[26]

18 February 2025 20:05:54

NSTX has a toroidal field that is approximately five times smaller and a β and electron Larmor radius that is 10 times larger than conventional tokamaks, yet the collisionality level is similar. Greater β values necessitate the inclusion of electromagnetic (EM) effects in the model, which may not be necessary in traditional tokamaks where β is not larger than the electron to ion mass ratio. Consequently, a new toroidal model is developed for electromagnetic ETG modes (EM-ETGMs) for NSTX and conventional tokamak plasmas. This new model will replace the current model in MMM that includes empirical scaling and only provides a formula for ETG thermal diffusivity.[3] The newly developed ETG model will be employed as a component of a more comprehensive transport module MMM in the integrated modeling code TRANSP to predict the time-dependent electron temperature profile in tokamak plasmas.

The remainder of this paper is organized as follows. Section II explains how the four field ETG model equations that govern the dynamics of low-frequency short- and long-wavelength electromagnetic toroidal ETG driven drift modes are derived. Section III describes the four different methods for calculating thermal diffusivities due to ETG modes. Section IV displays the simulation results as well as the methodology used to obtain these results. Section V is devoted to the results summary and discussion.

II. ETG MODEL EQUATIONS

The new ETG model includes new significant plasma-parameter dependencies. Although the ETG modes at the electron gyroradius scale are essentially electrostatic, electromagnetic effects in high β tokamak plasmas must be taken into account when β is greater than electron to ion mass ratio. The inclusion of electromagnetic effects will allow for the coupling of drift and Alfvén waves. This newly developed model is based on two-fluid equations governing the dynamics of low-frequency short- and long-wavelength electromagnetic ETG-driven drift modes. The Braghinski equations presume the dominance of collisions. However, collision dominance does not exist at the ETG mode frequency. Using fluid theory when collision dominance is not dominant demands a precise fluid closure. The fluid theory is applied without any expansion, preserving the fluid resonances caused by magnetic drifts.[27,28] The four field model equations are given below that govern the dynamics of low-frequency ($\omega \ll k_\parallel v_{Te}$) electromagnetic toroidal ETG driven drift modes. The equations includes the effects of density, temperature, and magnetic field perturbation and gradients, electron inertia, curvature, collisionality, non-circular flux surface, non-adiabatic ions, density dilution, Shafranov shift, gradient of β (β'), magnetic drift resonances and drift reversal, low and reverse magnetic shear, and $\mathbf{E} \times \mathbf{B}$ flow shear. Non-adiabatic ion effects, including $\mathbf{E} \times \mathbf{B}$ and polarization drifts, are taken into account without including ion temperature fluctuations. The effect of trapped electrons is ignored because the mode frequency is comparable to the bounce frequency (ω_{be}) and the conditions for the trapped electron mode participation ($\omega \ll \omega_{be}$) are not fulfilled. The magnetosonic perturbations in the model are ignored, but some of their effects are preserved through $\beta' = \partial \beta / \partial \rho$ and the magnetic drift frequency, where ρ is proportional to the square root of toroidal flux.

The electron continuity takes into account the $\mathbf{E} \times \mathbf{B}$ drift, diamagnetic drift, polarization drift, stress tensor drift, and parallel electron flow velocity, the latter of which is determined using Amperés law. The electron continuity equation is

$$\frac{\partial n_e}{\partial t} + \nabla \cdot (n_e \mathbf{V}_e) = 0, \tag{1}$$

where n_e is the electron density and $\mathbf{V}_e$ is the electron velocity, given by the sum of various drifts and parallel electron flow velocity

$$\mathbf{V}_e = \mathbf{V}_E + \mathbf{V}_{e*} + \mathbf{V}_{ep} + \mathbf{V}_{e\Pi} + \mathbf{V}_{e\parallel}. \tag{2}$$

The components of Eq. (2) are defined as follows. First, the $\mathbf{E} \times \mathbf{B}$ drift ($\mathbf{V}_E$) is given by

$$\mathbf{V}_E = \frac{c}{B_0^2} \mathbf{E} \times \mathbf{B},$$

in which c is the speed of light, B_0 is the equilibrium magnetic field, $\mathbf{E}$ is the electric field,

$$\mathbf{E} = -\nabla \phi - \frac{1}{c} \frac{\partial A_\parallel}{\partial t},$$

and $\mathbf{B}$ is the magnetic field,

$$\mathbf{B} = \nabla \times \mathbf{A},$$

where ϕ is the electrostatic potential and $\mathbf{A}$ ($A_\parallel$) is the vector potential (parallel to the magnetic field).

The diamagnetic drift ($\mathbf{V}_{e*}$) is given by

$$\mathbf{V}_{e*} = -\frac{c}{en_e B_0^2} \mathbf{B} \times \nabla p_e,$$

where e is the electronic charge, $p_e = n_e T_e$ is the electron pressure, and T_e is the electron temperature.

The magnetic drift ($\mathbf{V}_{eD}$) can be written as ∇B plus curvature ($(\hat{\mathbf{e}}_\parallel \cdot \nabla)\hat{\mathbf{e}}_\parallel$) drift, which is obtained as a result of fluid drift compressibility,

$$\mathbf{V}_{eD} = -\frac{cT_e}{eB_0} \hat{\mathbf{e}}_\parallel \times \left(\nabla \ln (B_0) + (\hat{\mathbf{e}}_\parallel \cdot \nabla)\hat{\mathbf{e}}_\parallel \right),$$

where $\hat{\mathbf{e}}_\parallel$ is the unit vector along the magnetic field.

The polarization drift ($\mathbf{V}_{ep}$) is given by

$$\mathbf{V}_{ep} = \frac{c}{B_0 \omega_{ce}} \frac{d\mathbf{E}}{dt},$$

where $d/dt = \partial_t + \mathbf{V}_e \cdot \nabla$ is the convective derivative.

Next, $\mathbf{V}_{e\Pi}$ is the stress tensor (Π) drift,

$$\mathbf{V}_{e\Pi} = -\frac{c}{en_e} \frac{\mathbf{B} \times \nabla \cdot \mathbf{\Pi}}{B_0^2}.$$

The electron velocity parallel to the magnetic field ($\mathbf{V}_{e\parallel}$) is calculated using Amperés law and by ignoring ion velocity parallel to the magnetic field,

$$\mathbf{V}_{e\parallel} = \frac{c}{4\pi en_e} \nabla_\perp^2 A_\parallel.$$

From these terms, we can obtain the following equation by inserting all the drift velocities and the parallel velocity into the electron continuity equation [Eq. (1)]. Afterward, we linearize them by assuming that all of the perturbed quantities are proportional to $\exp[i(\mathbf{k} \cdot \mathbf{r} - \omega t)]$ and use ($\partial_t = -i\omega, \nabla = ik$), where $\mathbf{k}$ is the wavevector and ω is the complex frequency,

$$(\omega - \omega_{\mathrm{De}})\hat{n}_e - \omega_{\mathrm{De}}\hat{T}_e - (\omega_{*e} - \omega_{\mathrm{De}} + k_\perp^2 \rho_e^2 (\omega - \omega_{*e}(1 + \eta_e)))\hat{\phi}$$
$$= -ck_\parallel k_\perp^2 \lambda_{\mathrm{De}}^2 \hat{A}_\parallel. \tag{3}$$

Here, $\omega = \omega_r + i\gamma$, where ω_r is the real frequency and γ is the mode's growth rate. The magnetic drift frequency (ω_{De}), diamagnetic drift (ω_{*e}), and Debye length (λ_{De}) are

$$\omega_{\mathrm{De}} = \frac{2T_e}{eB_u} k \cdot B_u \times \kappa, \quad \omega_{*e} = \frac{k_y T_e g_{ne}}{eB_u R}, \quad \lambda_{\mathrm{De}}^2 = \frac{T_e}{4\pi n_e e^2},$$
$$B_u = \frac{B_0 \rho d\rho}{r dr}, \quad \rho = \sqrt{\frac{2\Psi_t}{B_0}},$$

where B_u is the effective magnetic field, κ is the curvature of the field line, R is the major radius, $k_\parallel$ is the parallel wavenumber, $k_\perp^2 = k_x^2 + k_y^2$ is the wavenumber perpendicular to the magnetic field, and Ψ_t is the toroidal flux.[29]

The normalized temperature gradient (g_{Te}), normalized electron density gradient (g_{ne}), ratio of electron temperature to electron density gradients (η_e), electron thermal velocity (v_{Te}), electron cyclotron frequency (ω_{ce}), and electron gyroradius (ρ_e) are defined as follows:

$$g_{Te} = -R\hat{x} \cdot \frac{\nabla T_e}{T_e}, \quad v_{Te} = \sqrt{\frac{T_e}{m_e}},$$
$$g_{ne} = -R\hat{x} \cdot \frac{\nabla n_e}{n_e}, \quad \omega_{ce} = \frac{eB_u}{m_e c},$$
$$\eta_e = \frac{g_{Te}}{g_{ne}}, \quad \rho_e = \frac{v_{Te}}{\omega_{ce}},$$

where r is the minor radius, B_0 is the magnetic field on the axis, m_e is the electron mass, and $\hat{x}$ is the unit vector in the radial direction. The hat quantities in Eq. (3) are the dimensionless form of the perturbed quantities ($\sim$) of electron density (n_e), electron temperature (T_e), electrostatic potential (ϕ), and parallel electromagnetic potential ($A_\parallel$),

$$\hat{n}_e = \frac{\tilde{n}_e}{n_e}, \quad \hat{T}_e = \frac{\tilde{T}_e}{T_e}, \quad \hat{\phi} = \frac{e\tilde{\phi}}{T_e}, \quad \hat{A}_\parallel = \frac{ec\tilde{A}_\parallel}{T_e}.$$

The electron density, n_e, is related to the density of hydrogenic ions, n_H, impurity ions, $n_Z = f_Z n_e$, and fast hydrogenic ions, $n_f = f_s n_e$, via charge neutrality. Depending on the combination of hydrogen isotopes employed in the experiment, n_H can represent the sum of the densities of hydrogen, deuterium, and tritium. The predominant ion in the NSTX is deuterium, with a small amount of hydrogen density, and the impurity is carbon. The normalized perturbed densities (such as $\hat{n}_e = \tilde{n}_e/n_e$) are then related by $\hat{n}_e = (1 - Z_z f_Z - f_s)\hat{n}_H$, where Z_z is the impurity charge and assuming that impurities and fast ions do not take part in the perturbation, i.e., $\hat{n}_f = 0$ and $\hat{n}_z = 0$.

The charge conservation equation is calculated using $\nabla \cdot J = e(n_i V_i - n_e V_e) = 0$, where J is the plasma current density and V_i is the ion velocity, which is the sum of $E \times B$ and ion polarization drift

$$V_i = V_E - \frac{c}{B_0 \omega_{ci}} \frac{\partial \nabla_\perp \phi}{\partial t}. \tag{4}$$

Using Eqs. (2) and (4), the following charge conservation equation can be obtained:

$$\omega k_\perp^2 \rho_s^2 \hat{\phi} + \omega_{\mathrm{De}}(\hat{n}_e + \hat{T}_e) + k_\perp^2 \rho_e^2 (\omega - \omega_{*e}(1 + \eta_e))\hat{\phi} = ck_\parallel k_\perp^2 \lambda_{\mathrm{De}}^2 \hat{A}_\parallel, \tag{5}$$

with

$$\rho_s = \frac{c_s}{\omega_{ci}}, \quad c_s = \sqrt{\frac{T_e}{m_i}}, \quad \omega_{ci} = \frac{Z_i e B_u}{m_i c},$$

where ρ_s is the ion Larmor radius, c_s is the sound speed, ω_{ci} is the ion cyclotron frequency, Z_i is the effective ion charge, and m_i is the ion mass.

The parallel electron momentum equation is driven by electromagnetic forces, various electron drifts, the electron pressure gradient, as well as by the thermal and frictional forces

$$m_e n_e (\partial_t + V_e \cdot \nabla) V_e$$
$$= -en_e\left(E + \frac{1}{c} V_e \times B\right) - \nabla p_e - n_e \nabla_\parallel T_e - n_e m_e \nu_{ei} V_{e\parallel}. \tag{6}$$

The following parallel momentum equation is obtained using Eq. (2) into Eq. (6) and Amperés law:

$$(\omega + i\nu_{ei})k_\perp^2 \rho_s^2 \frac{v_A^2}{v_{Te}^2} \hat{A}_\parallel$$
$$= ck_\parallel \left(\hat{\phi} - \hat{n}_e - \hat{T}_e + \frac{\omega_{*e}(1 + \eta_e) - \omega}{ck_\parallel} \hat{A}_\parallel\right), \tag{7}$$

where ν_{ei} is the electron ion collision frequency and $v_A = B_0 / \sqrt{4\pi n_i m_i}$ is the Alfvén velocity.

Next, $\hat{T}_e$ is determined by the electron energy equation. The perpendicular fluid resonance is taken into account by the inclusion of electron diamagnetic heat flow,

$$\frac{3}{2}(\partial_t + V_e \cdot \nabla)T_e - \frac{T_e}{n_e}(\partial_t + V_e \cdot \nabla)n_e = -\frac{1}{n_e} \nabla \cdot q_e, \tag{8}$$

where q_e is the combination of frictional, thermal gradient, and the cross field electron heat fluxes,

$$q_e = 0.71 n_e T_e (V_e - V_i) + \frac{3.2 n_e T_e}{m_e \nu_{ei}} \nabla_\parallel T_e + \frac{5}{2} \frac{c n_e T_e}{eB_0} \hat{e}_\parallel \times \nabla T_e. \tag{9}$$

The following energy equation for collisional plasma can be produced by using Eqs. (2) and (9) into Eq. (8):

$$\left(\omega - \frac{5}{3}\omega_{\mathrm{De}} + ik_\parallel^2 D_e\right)\hat{T}_e$$
$$= \left(\eta_e - \frac{2}{3}\right)\omega_{*e}\hat{\phi} + \frac{2}{3}\omega\hat{n}_e - \frac{2}{3}ck_\parallel k_\perp^2 \lambda_{\mathrm{De}}^2 \hat{A}_\parallel + ik_\parallel^2 D_e \eta_e \frac{\omega_{*e}}{ck_\parallel}\hat{A}_\parallel, \tag{10}$$

where $D_e = \frac{2T_e}{m_e \nu_{ei}}$. This energy equation incorporates both convective and compressional effects, collisional effects, as well as fluid resonance. Note that the ETG model Eqs. (3), (5), (7), and (10) are valid in the frequency regime $\omega \sim \omega_{\mathrm{De}}, \sim \omega_{*e}, \sim \omega_A$, where $\omega_A = k_\parallel v_A$ is the Alfvén frequency. These coupled equations describe the dynamics of toroidal electromagnetic waves in non-uniform magnetic fields and in inhomogeneous electron-ion plasmas. Note that Eq. (10) can readily take the following usual equation of state in a low collisionality regime:

$$\hat{T}_e = \eta_e \frac{\omega_{*e}}{ck_\parallel} \hat{A}_\parallel. \tag{11}$$

It is also worth noting that for large $k_\perp \rho_s$ and for low collisionality region, electromagnetic effects take precedence, as evidenced by the

scans presented in Sec. IV. In the limit $\omega_{\mathrm{De}} \gg \omega_A, \omega_{*e}$ and in the absence of a perturbed magnetic field, Eq. (3) can take the form $\hat{n}_e = \hat{\phi}$, which corresponds to electron thermalization along the field line. Note that the Braginskii equations presume the dominance of collisions. However, collision dominance does not exist at the ETG mode frequency. Using fluid theory when collision dominance is not dominant demands a precise fluid closure. Thus, a fluid theory is applied without any expansion, preserving the fluid resonances caused by magnetic drifts.[27,28]

The perpendicular and parallel operators $k_\perp$, $k_\parallel$, and ω_{De} in $s - \alpha_{\mathrm{m,u}}$ geometry can be written as

$$k_\perp^2 = k_\theta^2(1 + (\hat{s}\theta - \alpha_{\mathrm{m,u}} \sin \theta)^2), \tag{12}$$

$$k_\parallel = \frac{-i}{qR}\frac{\partial}{\partial \theta}, \tag{13}$$

$$\omega_{\mathrm{De}} = \frac{2k_\theta T_e}{eB_u R} g(\theta), \tag{14}$$

$$g(\theta) = \cos \theta + (\hat{s}\theta - \alpha_{\mathrm{m,u}} \sin \theta)\sin \theta - \frac{\alpha_{\mathrm{m,u}}}{2q^2}, \tag{15}$$

where q is the safety factor, θ is the extended angle, and $\alpha_{\mathrm{m,u}}$ is the ballooning parameter

$$\alpha_{\mathrm{m,u}} = \frac{2\mu_0 Rq^2}{B_u^2}\frac{dp}{dr} = q^2 \beta_{e,u}\left(g_{ne} + g_{Te} + \frac{p_i}{p_e}(g_{Ti} + g_{ni})\right), \tag{16}$$

where $\beta_{e,u} = \mu_0 p_e/B_u^2$ is the electron pressure p_e to magnetic pressure B_u^2/μ_0 and p_i is the ion pressure.

The perpendicular wave-number of ETG drift wave turbulence in Eq. (12) is dependent on the ballooning parameter ($\alpha_{\mathrm{m,u}}$) and the effective magnetic shear ($\hat{s}$), which is defined as

$$\hat{s} = \pm\sqrt{2s - 1 + (a\nabla\hat{\rho})^2(s-1)^2}. \tag{17}$$

Note that $\hat{s} = s$ for circular geometry ($a\nabla\hat{\rho} = 1$), where $s = (r/q)(dq/dr)$.

Reference 30 shows the limiting case of Eq. (17), in which just the effects of elongation are addressed. The reason we use this formula for effective magnetic shear ($\hat{s}$) rather than shear (s) is to include general geometrical effects in the ETG model. When adding general geometry, the main effect is to change the perpendicular wave vector so that it can differ due to the toroidal flux. It is the variation of the toroidal flux inside the flux surface that is significant as we move toward the plasma edge along the radius, e.g., the flux surfaces will move closer together with increasing elongation. This will enter the wavevector as an effective increase in the magnetic shear. However, the effects of general geometry ($\nabla\hat{\rho}$), such as triangularity and elongation, are included through their effects on the area of the local cross section.

Knowledge of the eigenfunction $\phi(\theta)$ is required to determine the precise dependence of the magnetic drift frequencies, $k_\parallel$ and $k_\perp$, on the ballooning parameters $\alpha_{\mathrm{m,u}}$ and $\hat{s}$. The result of a basic trial function averaged over the ballooning space is used.[10]

Note that while conventional ETG modes are short wavelength ($k_y\rho_s \gg 1.0$) with adiabatic ions, non-adiabatic ion effects are taken into account in the new EM-ETGM. The mode frequency is comparable to both the ion magnetic and electron drift frequencies, which ensures that the assumption of ion adiabaticity is not used. These

non-adiabatic effects may provide stabilizing effects to the ETG modes even before drift reversal occurs. Conventional ETG modes have frequency on the order of $\omega \gg k_\parallel v_{\mathrm{Te}}$, whereas these modes have frequency on the order of $\omega \ll k_\parallel v_{\mathrm{Te}}$. Furthermore, conventional ETG modes are generally electrostatic and can be stabilized by large β.[3,16] On the other hand, the ETG modes reported in this study are found to be unstable in almost all NSTX discharges considered, despite the fact that NSTX discharges are known to have large β values. Moreover, these ETG modes, unlike microtearing modes, are short wavelength ($k_y\rho_s \geq 1.0$) modes that exist even when there is no collisionality and electron inertia and their growth rate resonate with magnetic drift frequency. The electromagnetic ETG mode is thought to be a toroidal version of the drift Alfvén mode, which becomes unstable even in the deep core region. This is due to charge separation caused by an unfavorable magnetic field gradient and curvature electron drift in the presence of an electron temperature and density gradient. The anomalous electron thermal diffusivity associated with the ETG model is calculated in Sec. III using a variety of methods and using quasilinear approximations. It is worth pointing out that quasilinear approximation works well in the fluid theory[28,31] but not in kinetic theory. Convective velocities are always particle velocities, such as $\mathbf{E} \times \mathbf{B}$ drift, Alfvén velocity, etc. The variation in temperature over time is calculated as $V_E\tilde{T}_e$. Thus, convection is a result of $\mathbf{E} \times \mathbf{B}$ drift. Our effective diffusivities also incorporate convection; no additional convection should be utilized.[32]

III. ELECTRON THERMAL DIFFUSIVITY

The electron thermal fluxes depend on ETG driven drift eigenvalues and eigenvectors. Heat flux is computed directly from the eigenvectors,

$$\Gamma = \tilde{T}_e\tilde{v}_E^* + \text{c.c.} = \frac{2k_y}{B_0}\left(\text{Re}(\tilde{T}_e)\text{Im}(\tilde{\phi}) - \text{Im}(\tilde{T}_e)\text{Re}(\tilde{\phi})\right). \tag{18}$$

The saturation level is estimated balancing linear growth rate with $\mathbf{E} \times \mathbf{B}$ non-linearity

$$\hat{\phi} \approx \frac{2\hat{\gamma}}{Rk_x}; \quad \hat{\gamma} \equiv \gamma\frac{\bar{G}}{\omega_{\mathrm{De}}}, \quad \bar{G} = \frac{2}{3} + \frac{5}{9}\hat{s} - \frac{5}{12}\alpha_{\mathrm{m,u}} - \frac{5}{4}\frac{\alpha_{\mathrm{m,u}}}{q^2}, \tag{19}$$

where $\hat{\phi}$ is used to compute the electron thermal flux, given by

$$\Gamma = \frac{4T_e\omega_{\mathrm{De}}}{Rk_x^2\bar{G}}\frac{\hat{\gamma}^2}{|\hat{\phi}|^2}\left(\text{Re}(\hat{T}_e)\text{Im}(\hat{\phi}) - \text{Im}(\hat{T}_e)\text{Re}(\hat{\phi})\right). \tag{20}$$

The eigenvalues yield the real frequency and growth rate of the mode while the eigenvectors provide the phase and magnitude of perturbed variables relative to one another. Electron thermal diffusivity is given by $\chi_e = -\Gamma/(dT_e/dr)$, which gives us

$$\chi_e = \frac{4\omega_{\mathrm{De}}}{g_{Te}k_x^2\bar{G}}\sum_j\frac{\hat{\gamma}_j^2}{|\hat{\phi}_j^2|}\left(\text{Re}(\hat{T}_e)_j\text{Im}(\hat{\phi})_j - \text{Im}(\hat{T}_e)_j\text{Re}(\hat{\phi})_j\right). \tag{21}$$

Note that the sum over j pertains to solutions obtained from each of the four equations given by Eqs. (3), (5), (7), and (10).

Alternatively, the electron energy equation provides another approach for calculating ETG electron thermal diffusivity. It employs the eigenvalues of the ETG modes but is independent of ETG

eigenvectors. This alternative electron thermal diffusivity formula can be written as

$$\chi_e^* = \frac{\omega_{De}}{g_{Te} k_x^2 \bar{G}} \left(g_{Te} - \frac{2}{3} g_{ne} + \frac{20}{9} g_{Bu} \right) \sum_j \frac{\hat{\gamma}_j^3}{\left(\hat{\omega}_j - \frac{5}{3}\bar{G}\right)^2 + \hat{\gamma}_j^2}, \quad (22)$$

where

$$\hat{\omega} = \omega_r \frac{\bar{G}}{\omega_{De}}, \quad g_{Bu} = R\hat{x} \cdot \frac{\nabla B_u}{B_u}.$$

The alternative electron thermal diffusivity formula for ETG modes in Eq. (22) is inferred from the ITG difusivity formula in Refs. 33 and 34 by swapping the roles of ions and electrons. The diffusivities provided by Eqs. (21) and (22) can each be handled in two different ways to provide a total of four different diffusivity formulations in the new EM-ETGM. First, choosing the k_y value corresponding to the most unstable mode at each radial location provides one diffusivity value from each equation. Second, a sum over k_y values within a chosen range can be computed at each radial location to provide a second diffusivity value from each equation. Generally, ETG modes have large k_y and smaller k_x; therefore, we have assumed that $k_x = \frac{1}{2}k_y$.[35] Note that modifying the estimation of k_x has a minimal impact on the form of the growth rate, but a significant impact on the magnitude of electron thermal diffusivity. This is why, if necessary, nonlinear gyrokinetic simulations will be used to calibrate the thermal diffusivity of electrons. Additionally, we have also considered a k_y range of $1 \leq k_y \rho_s \leq 50$ at each radial point. The scans in Sec. IV are performed to study the dependence of ETG real frequency, growth rate, and diffusivity on various plasma parameters. It is worth pointing out that quasilinear approximation works well in fluid theory[28,31] but not in the kinetic theory. Convective velocities are particle velocities, such as $\mathbf{E} \times \mathbf{B}$ drift, Alfvén velocity, etc. The variation in temperature over time is calculated as $V_E \bar{T}_e$. Thus, convection is a result of $\mathbf{E} \times \mathbf{B}$ drift. Our effective diffusivities also incorporate convection. No additional convection should be utilized.[32]

IV. SIMULATION RESULTS

The data of low collisionality NSTX discharge 138 536 at time $t = 0.629$s is used to scan the plasma parameter dependence on the ETG real frequency, growth rate, and electron thermal diffusivity. A $k_y \rho_s$ scan is carried out to find the most unstable mode at each normalized radial label $\hat{\rho}$. The NSTX experimental plasma parameters are varied throughout the radius to produce peaked and flat density, low and high β, collisionality, electron temperature, electron density, positive- and reverse-magnetic shear, and low and high safety factor scans. In addition, the results are compared with and without collisions, electromagnetic effects, flow shear, density gradient, and temperature gradients.

The parameter scans were conducted by multiplying experimental input profiles by a range of factors at each radial point. Both a direct and indirect approach was used to apply the range of multipliers to target parameters. In the direct approach, the value of the target parameter was adjusted directly in the MMM code,[25,36] without modifying any of the input variable values related to that parameter. Alternatively, the indirect approach involved modifying the input variables used to derive the target parameter. In some cases, these two approaches were equivalent as the target parameter was also an input

variable. These scans were conducted using 101 radial points for input values along with at least 100 different multiplier values for varied parameters, which resulted in each contour plot containing over 10 000 points of data. Additional details specific scan methodology is given at the beginning of each corresponding subsection.

A. Electron temperature gradient

The electron temperature gradient scan was carried out by modifying the experimental value of g_{Te} without adjusting any other input variables. A multiplier is then used to increase and decrease the experimental g_{Te} value. The discovery of the growth rate in the deep core region and destabilizing effects of g_{Te} is shown in Fig. 1(b). The multiplier of 1.0 on the y-axis of each contour plot corresponds to experimental values. For this scan, the growth rate increases as g_{Te} increases and decreases as g_{Te} decreases. The mode is found to be stable when the experimental value of g_{Te} is increased by a factor of 2.4 around $\hat{\rho} \approx 0.2$, due to the drift reversal. As g_{Te} increases, so does $\alpha_{m,u}$, which shifts the sign of the magnetic drift frequency from positive to negative and stabilizes the mode. In Fig. 1(d), the negative region of the magnetic drift frequency is represented by the white region. The unstable modes in the deep core region indicate the presence of electron thermal transport. The Alfvén frequency in Fig. 1(e) is found to be comparable to the real frequency in Fig. 1(c), which indicates that the magnetic fluctuations are due to short-wavelength Alfvén modes in the deep core region and are present for finite temperature gradient. The possibility of the existence of electromagnetic instability in the deep core region of NSTX discharges is also indicated in Refs. 16 and 37. The growth rate of ETG modes is found to be about the same in magnitude as the real frequency, which indicates a strong instability. Moreover, the ETG mode is found to propagate in the electron diamagnetic direction with a positive real frequency. The mode is found to be stable near the magnetic axis and close to the edge for $\omega_{De} > \omega$, and $k_y \rho_s \gg 1.0$ because the dynamics may become adiabatic.

The contour plots of growth rate and real frequency are shown in Figs. 1(g) and 1(h) for $g_{ne} = 0$. It is found that the drift reversal occurs earlier around $\hat{\rho} \approx 0.2$ in the presence of g_{ne} as compared to the $g_{ne} = 0$ case, so very large values of g_{ne} can be stabilizing. However, the growth rate is not found to be very different with or without g_{ne} for $\hat{\rho} \geq 0.35$. This implies that the destabilizing effects of nonzero g_{ne} on the growth rate for $\hat{\rho} > 0.35$ are weak. On the other hand, the $g_{Te} = 0$ case in Fig. 1(i) substantially decreases the growth rate when compared with the default case $(g_{Te}, g_{ne} \neq 0)$, implying that the mode is less dependent on the plasma parameter η_e.

B. Electron density gradient

The electron density gradient scan shown in Fig. 2 was performed by changing the experimental value of g_{ne} without changing any other input variables. Positive g_{ne} is discovered to be destabilizing, whereas negative g_{ne} is discovered to be stabilizing. The growth rate is found to be increasing with increasing g_{ne} particularly in the region $\hat{\rho} \approx 0.7$, where temperature gradient is also large. Large g_{ne} is stabilizing for the short wavelength Alfvén eigenmode at $\hat{\rho} \approx 0.2$ due to g_{ne} drift reversal which indicates the toroidal nature of the mode. The increase in the density gradient caused by pellet injection[38] has been seen in the experiments and can be used as a knob to stabilize these modes.[39]
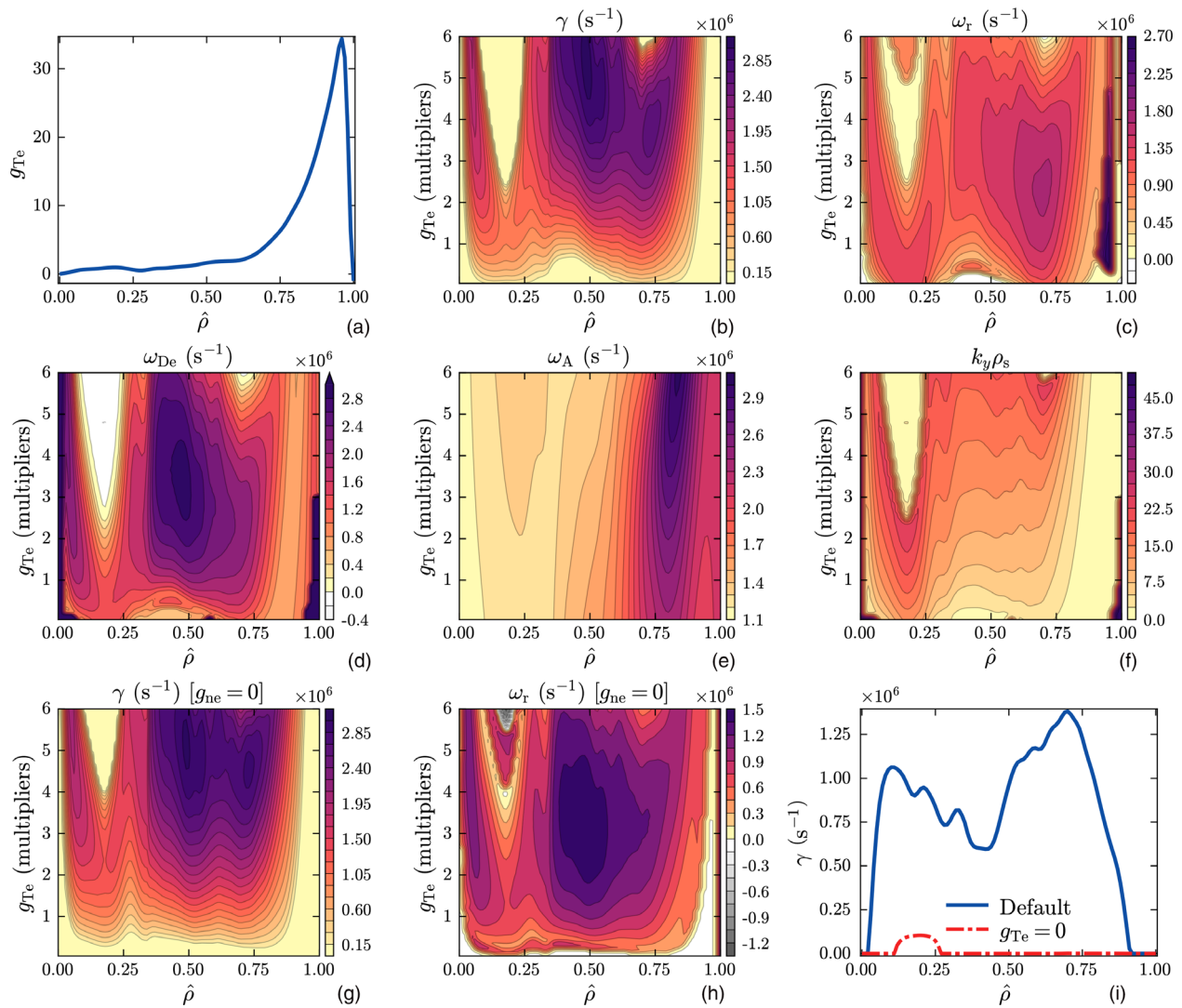
FIG. 1. (a) The experimental normalized electron temperature gradient (g_{Te}). Contours of (b) growth rate, (c) associated real frequency, (d) magnetic drift frequency (ω_{De}), (e) Alfvén frequency (ω_A), (f) $k_y\rho_s$, (g) growth rate with $g_{ne} = 0$, (h) corresponding real frequency with $g_{ne} = 0$, and (i) growth rate using experimental values with and without $g_{Te} = 0$. The ETG modes are found unstable in the region $\hat{\rho} \leq 0.4$ due to electromagnetic effects, whereas conventional electrostatic ETG modes have often been found to be stable in this region of the NSTX discharges.

However, pellet injection is not available in the NSTX tokamak. Note that this NSTX discharge goes edge-localized modes (ELM)-free after between-shots lithium wall conditioning. These types of ELM-free discharges tend to accumulate carbon impurity sourced from the plasma facing components, which can lead to transient peaking in the outer region. Consequently, it is possible to obtain a non-monotonic electron density profile [Fig. 6(a)], which results in the region of negative g_{ne} seen in Figs. 2(a) and 2(b). No unstable mode is found in Fig. 2(e), where $g_{Te} = 0$ and $g_{ne} \leq 0$. The mode is found to be less unstable in the negative g_{ne} region around $\hat{\rho} \approx 0.45$ and becomes stable around $\hat{\rho} \approx 0.4$ when $g_{Te} = 0$. As seen in Fig. 2(f), the effects of $g_{ne} = 0$ on the growth rate are less than those of $g_{Te} = 0$ as seen in Fig. 2(e) and

previously in Fig. 1(i), which show that the modes are more dependent on g_{Te} than η_e.

In summary of Subsections IV A and IV B, for electromagnetic ETG modes, there are three drives or sources of free energy: (i) electron temperature gradient, (ii) electron density gradient, and (iii) ∇B plus curvature drift. For nonzero gradients and due to bad curvature, the deep core exhibits electromagnetic ETG instability. The electron temperature gradient has a greater influence on the modes than the electron density gradient. The magnitude and frequency of the growth rate are found to be comparable, which indicates a strong instability. Large g_{ne} (peaked density profile) provides stabilizing effects on short wavelength modes, which is consistent with the results in Ref. 24.
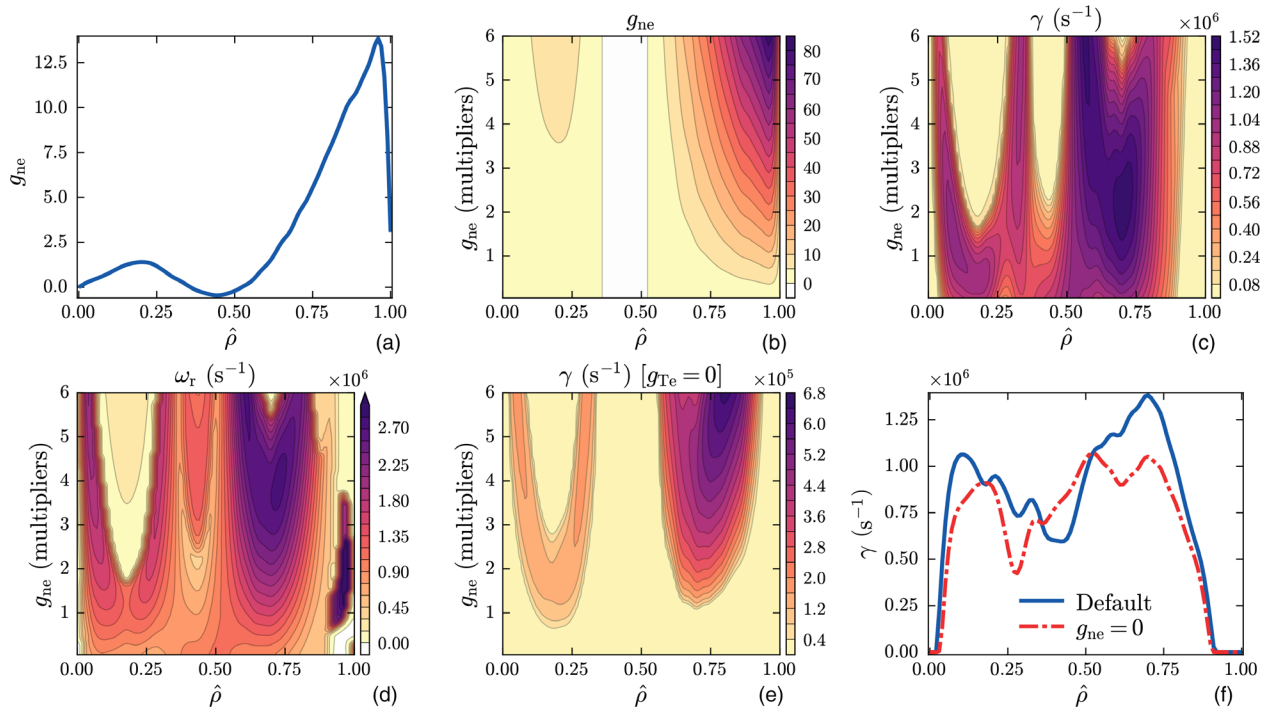
FIG. 2. (a) The experimental normalized electron density gradient (g_{ne}). Contours of (b) variation of g_{ne}, (c) growth rate (d) associated real frequency, (e) growth rate with $g_{Te} = 0$, and (f) growth rate at experimental value with or without $g_{ne} = 0$. The effect of positive g_{ne} is destabilizing, while negative g_{ne} is stabilizing.

C. Safety factor

The q profile scan is carried out by multiplying the experimental q profile shown in Fig. 3(a) by a range of factors at each radial point, without changing any other input variables. The ETG growth rate and frequency of the modes shown in Figs. 3(b) and 3(c) increase with increasing q, with the exception of around $\hat{\rho} = 0.2$, where Alfvén modes are present. Large values of q are stabilizing and small values of q are destabilizing for this drift Alfvén mode, due to the electromagnetic nature of these modes. NSTX-U will use a higher magnetic field when going to higher current, so q would not drop as much; otherwise, there will likely be some severe MHD stability/disruption limits.

This suggests that these modes exist even in updated NSTX (NSTX-U) plasmas with an increased plasma current from $I_p = 1.1 \rightarrow 2.0$MA. The growth rate is found to be smaller around $\hat{\rho} = 0.45$ due to negative density gradient in this region.

The effects of small q on ETG modes are stabilizing for $\hat{\rho} > 0.45$ because electromagnetic effects decrease as $\hat{\rho}$ increases, and the mode's characteristics change from Alfvén to conventional ETG modes whose growth rates increase with increasing q and produce a more ballooning nature. This implies that in high current NSTX-U discharges, these modes will be less destabilizing. A drift reversal is also evident around $\hat{\rho} \approx 0.2$ and 0.7 due to large values of q. The magnetic drift frequency
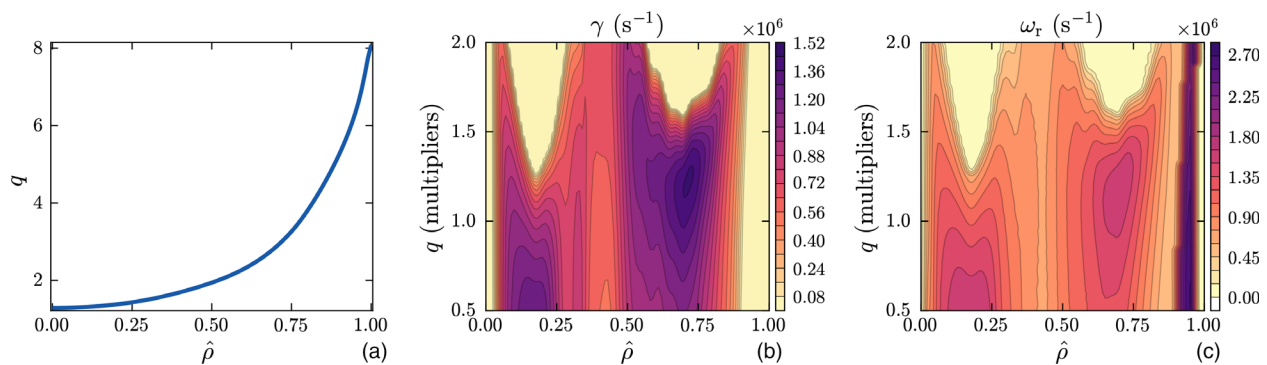
FIG. 3. (a) The experimental safety factor (q) profile; contours of (b) growth rate and (c) associated real frequency. The ETG mode is found to be substantially destabilized when q is increased.

(ω_{De}), which is not shown here, coincides with the drift reversal, indicating that the growth rate resonates with ω_{De}.

D. Effective magnetic shear

The effective magnetic shear ($\hat{s}$) in Eq. (17) is varied indirectly by varying magnetic shear (s) at each radial point, without modifying any other input variables. The experimental magnetic shear and effective magnetic shear are plotted in Fig. 4(a). According to the growth rate shown in Fig. 4(b), the ETG mode is found to be substantially stabilized when the effective magnetic shear $\hat{s}$ is reversed.[14] Effective magnetic shear is also nearly constant for $\hat{\rho} < 0.2$ due to shear being negligible in this region. The growth rate and frequency of the ETG mode are found to be decreasing with both increasing magnetic shear and reverse magnetic shear. The effective magnetic shear is expected to increase as NSTX-U elongation and triangularity increase, resulting in a decrease in the ETG mode growth rate. As shown in Figs. 4(e) and 4(f), the electrostatic potential grows toward the edge, whereas the electromagnetic potential rises in the core, indicating that modes in the center are more electromagnetic in nature. The magnetic drift frequency changes sign as effective magnetic shear changes sign. The stabilizing effects of reverse magnetic shear[40] will suppress electron thermal transport, which is responsible for the ITB region[41] in the electron temperature profile of NSTX discharges.

In summary of Subsections IV C and IV D, the electromagnetic ETG modes (EM-ETGMs) are found to stabilize with increasing q in the core, where the modes are electromagnetic in nature. On the other hand, significant destabilization is seen in the confinement region, where the modes are more electrostatic in character; this trend is similar to the conventional ETG modes. Large and reverse magnetic shear effects on EM-ETGM are found to be stabilizing, which can lead to ITB in the electron temperature profile. These results are found to be in line with those in Refs. 42 and 43.

E. Electron temperature

The electron temperature scan is carried out by multiplying the experimental T_e profile shown in Fig. 5(a) by a range of factors at each radial point, without changing any other input variables. Figures 5(a)–(f) depict the dependence of electron temperature variation on the EM-ETGM growth rate, $k_y\rho_s$, $|\hat{A}_{\parallel}|^2$, real frequency, and ω_{De}. The increasing and decreasing trends of the growth rate and real frequency at different radial locations are similar. EM-ETGM is found to be destabilizing when T_e is increased except near $\hat{\rho} = 0.2$. Increasing T_e, while maintaining constant normalized temperature gradients at each $\hat{\rho}$, increases $\alpha_{m,u}$ via $\beta_{e,u}$ and decreases ν_{ei}. However, increases in $\alpha_{m,u}$ are slow because T_i/T_e decreases with increasing T_e. Figure 6(d) illustrates that T_i/T_e is not always greater than one and that T_i/T_e decreases rapidly as T_e increases. Increasing $\alpha_{m,u}$ stabilizes the Alfvén modes around $\hat{\rho} = 0.2$ and enhances the growth of the modes at other radial locations including $\hat{\rho} < 0.2$. Alfvén mode stabilization can be achieved when the experimental T_e is multiplied by 1.5, while the ETG mode stabilization is found when the experimental T_e is multiplied by 3.5. Additionally, increasing $\alpha_{m,u}$ makes curvature favorable ($\omega_{De} < 0$). The large values of $|\hat{A}_{\parallel}|^2$ in the center indicate the
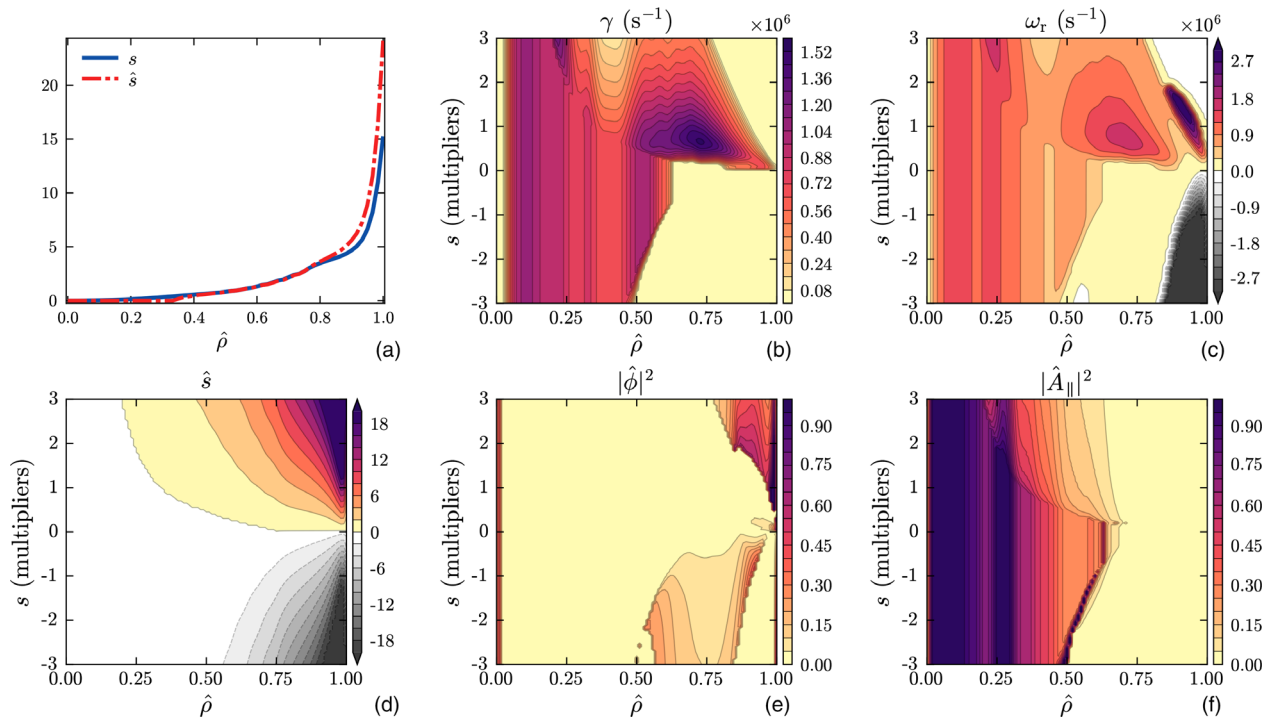
FIG. 4. (a) The magnetic shear (s) and effective magnetic shear ($\hat{s}$) are plotted vs $\hat{\rho}$. Contours of (b) growth rate, (c) real frequency, (d) effective magnetic shear, (e) square of the normalized potential ($|\hat{\phi}|^2$), and (f) square of the normalized vector potential ($|\hat{A}_{\parallel}|^2$). The ETG mode is found to be substantially stabilized when $\hat{s}$ is reversed.
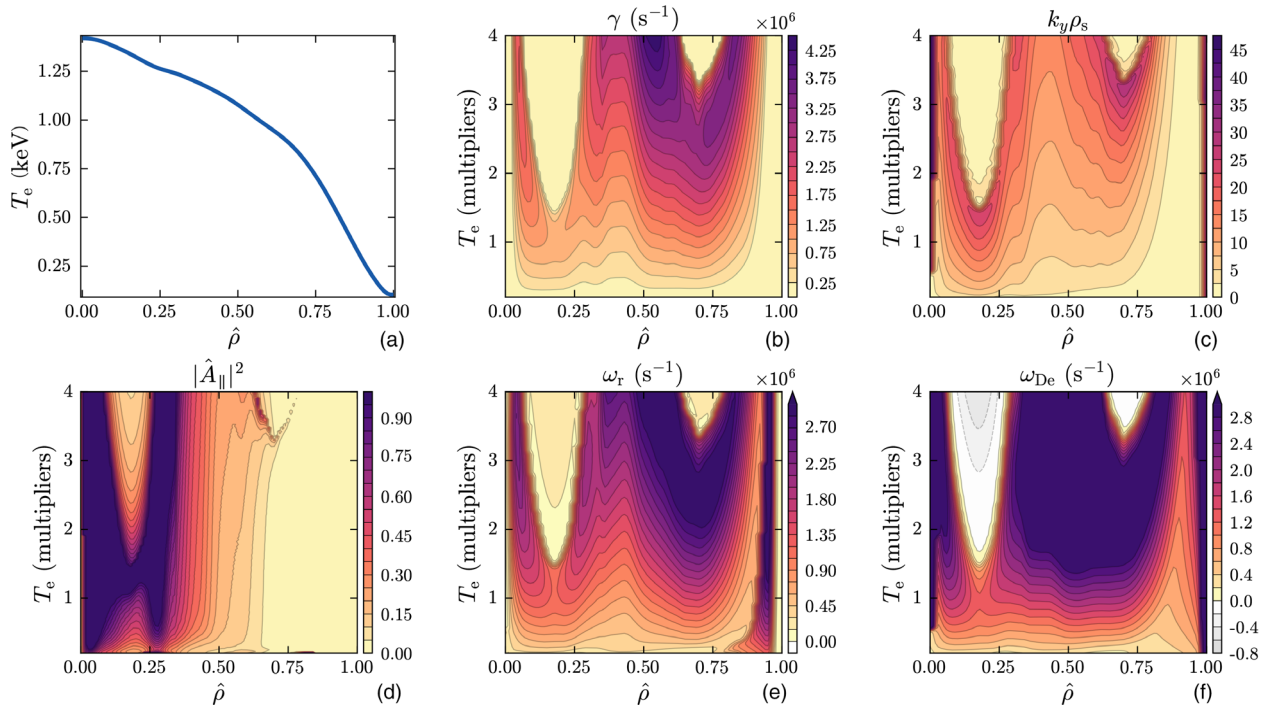
FIG. 5. (a) The experimental electron temperature profile. Contours of (b) growth rate, (c) $k_y \rho_s$, (d) square of the normalized vector potential ($|\hat{A}_{\parallel}|^2$), (e) real frequency, and (f) magnetic drift frequency (ω_{De}). EM-ETGM is found to be destabilizing when T_e is increased, except in the deep core region.
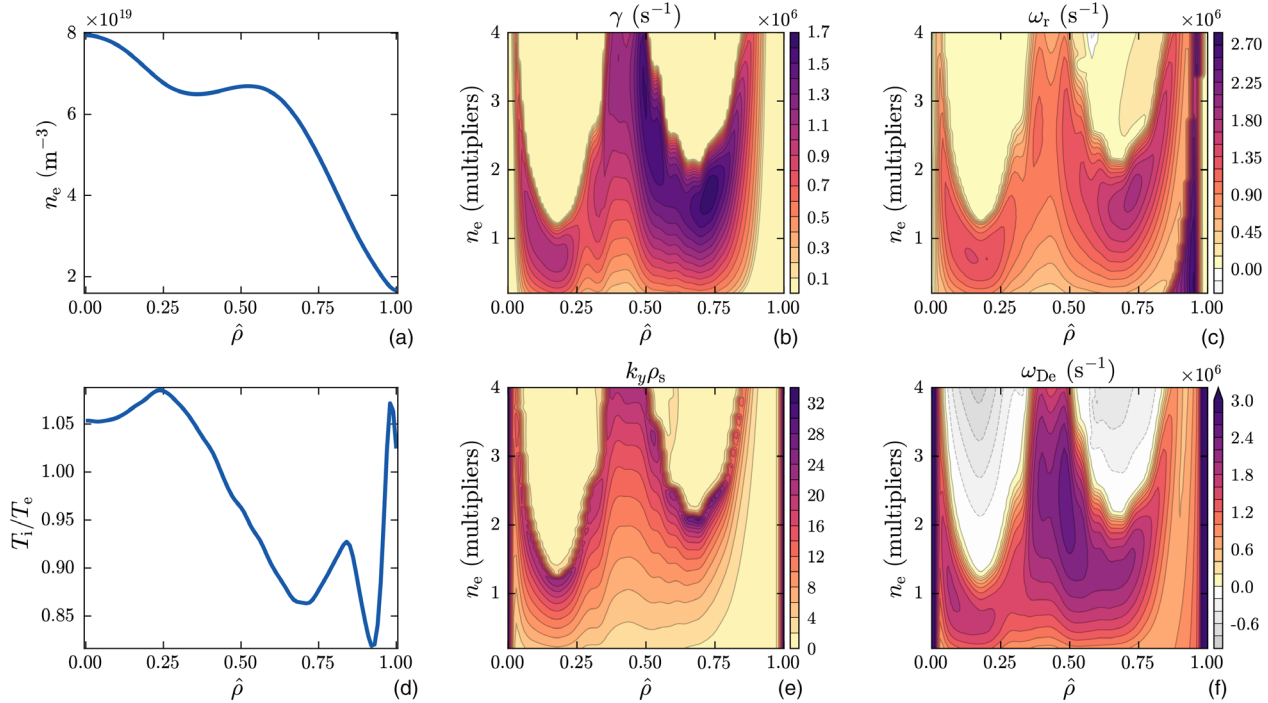
FIG. 6. (a) The experimental electron density profile. Contours of (b) growth rate and (c) real frequency. (d) The ion to electron temperature ratio, contours of (e) $k_y \rho_s$ and (f) magnetic drift frequency (ω_{De}). EM-ETGM is found to be stabilized when n_e is substantially increased in the large density gradient regions.

electromagnetic characteristic of the mode. The EM-ETGM growth rate is found to be high for large $k_y \rho_s$ values.

F. Electron density

The electron density scan was carried out by modifying the experimental value of n_e in the input file. The values of the impurity density, hydrogenic density, fast ion density, and thermal ion density were likewise modified by the same factors to obey quasi-neutrality in order to maintain self-consistency among these variables. Otherwise, all of the other remaining input variables remained unchanged. Figure 6 depicts the dependence of electron density n_e on the EM-ETGM growth rate and real frequency. The experimental electron density profile, ion-to-electron temperature ratio profile, $k_y \rho_s$, and ω_{De} contour plots are also displayed.

EM-ETGM is found to be stabilizing when n_e is substantially increased in the large density gradient regions. Increasing n_e increases $\alpha_{m,u}$ via $\beta_{e,u}$ and also increases ν_{ei}. Increasing $\alpha_{m,u}$ has a stabilizing effect, except near $\hat\rho \approx 0.4$ and close to the axis where g_{ne} is small and drift reversal ($\omega_{De} < 0$) does not occur. Drift reversal is also not found around $\hat\rho \approx 0.8$, where the temperature ratio is small. The EM-ETGM growth rate and real frequency both increased with increasing $k_y \rho_s$ at first, then decreased for larger values of $k_y \rho_s$, indicating a typical non-monotonic trend of the drift wave growth rate with $k_y \rho_s$.

G. Magnetic field

The experimental B_u value at each surface is multiplied by a range of values to show B_u dependency on ETG modes, without changing any other input variables. Figure 7 depicts the relationship between the effective magnetic field (B_u) and the EM-ETGM growth rate and real frequency. The most unstable ETG mode is determined by performing a $k_y \rho_s$ scan on each surface.

The mode is found to be stabilized for large values of B_u and destabilized for small values of B_u. This indicates that the rate these modes grow might be slower in NSTX-U plasmas than in NSTX due to NSTX-U plasmas having a larger B-field. However, our results did not show complete mode stabilization or drift reversals as a result of increasing B_u.

H. Electron beta

In Secs. IV E–IV G, the electron temperature, electron density, and magnetic field were all varied independently about their experimental values. The electron beta ($\beta_{e,u}$) scan is performed, and its relationship to the EM-ETGM growth rate and frequency is depicted in Fig. 8. The results presented here are from the indirect approach, in which the electron temperature and density, as well as the magnetic field input variables, were all varied to target the electron beta. Variables affected by electron density were also modified in accordance with the electron density scan in Sec. IV F. A direct scan of $\beta_{e,u}$ was also performed (not shown here), and the results are found to be nearly identical to the results of the indirect input variable scan shown here.

The experimental $\beta_{e,u}$ value at each surface is multiplied by a range to show $\beta_{e,u}$ dependency on ETG modes. EM-ETGM shows a non-monotonic $\beta_{e,u}$ dependence. The growth rate of modes increases initially as $\beta_{e,u}$ increases and then decreases as $\beta_{e,u}$ increases further. Drift reversal occurs as a result of high $\beta_{e,u}$ values. Drift reversal also occurs for toroidal drift Alfvén modes when the experimental value of $\beta_{e,u}$ is increased by a factor of 1.4. However, drift reversal does not occur in regions with a negative density gradient and a low ion-to-electron temperature ratio. The frequency of the mode is comparable to the growth rate and is observed to behave similarly.

In summary of Secs. IV E–IV H, the EM-ETGM growth rate increased with increasing T_e and n_e at first, then decreased as they increased, demonstrating a non-monotonic drift wave growth rate. This implies that plasmas with low collisionality will be more destabilized. The large magnetic field and small $\beta_{e,u}$ are found to be EM-ETGM stabilizers. Note that when a scan of a toroidal magnetic field is performed, neither the equilibrium nor the q-profile are modified. However, $\beta_{e,u}$ does change. It has been discovered that a large magnetic field is stabilizing, but a small magnetic field is destabilizing. Because $\beta_{e,u}$ is inversely proportional to the square of the magnetic field, a large $\beta_{e,u}$ is found to be destabilizing, whereas a small $\beta_{e,u}$ is stabilizing.

I. Electromagnetic effects

An electromagnetic vs electrostatic comparison was carried out in Fig. 9(a) by removing the electromagnetic potential terms from the EM-ETGM model equations. Turning off $A_\parallel$ effects reduced overall EM-ETGM growth rate and stabilized the mode in the deep core of the low shear and low $\hat{s}/q$ region. When electromagnetic effects are turned off, the electrostatic ETG mode is found to be unstable for $\hat\rho > 0.35$. Modes with electromagnetic inclusion have both electrostatic and electromagnetic properties when $\hat\rho > 0.35$ and have
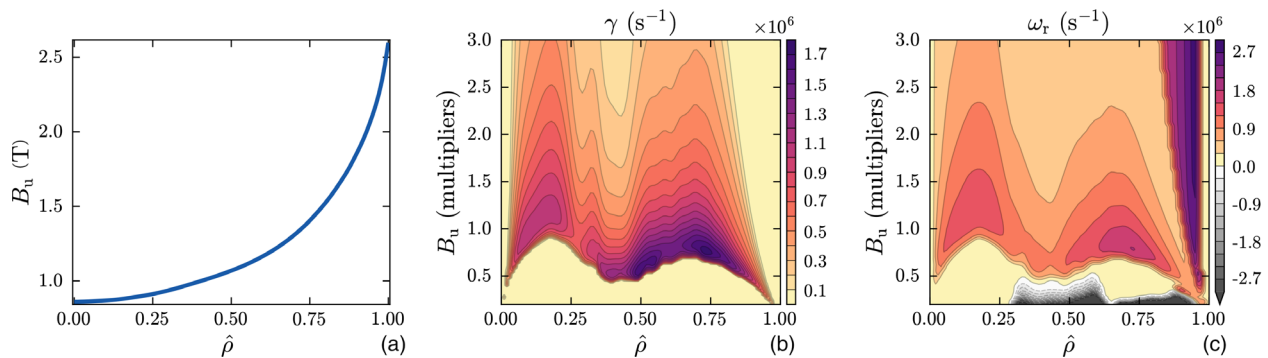
FIG. 7. (a) The effective magnetic field (B_u) profile. Contours of the EM-ETGM (b) growth rate and (c) real frequency. Large magnetic field is found to be stabilizing, but small magnetic field is destabilizing.
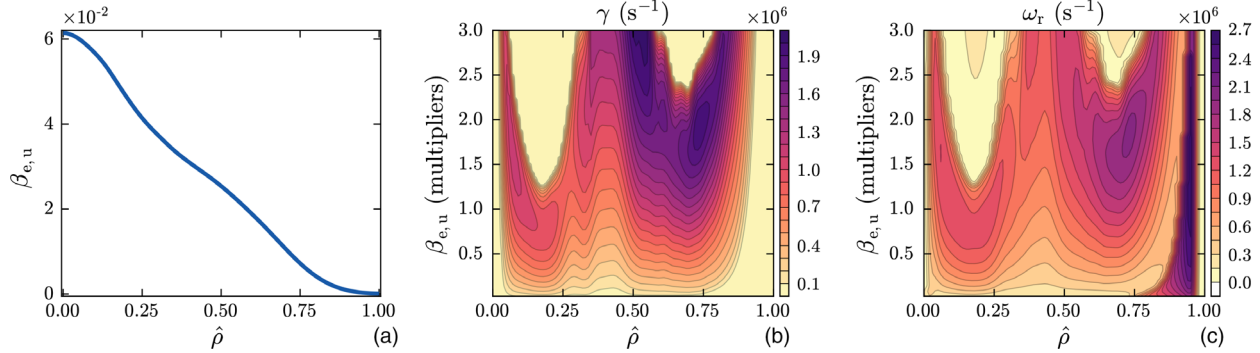
FIG. 8. (a) The experimental profile of electron beta ($\beta_{e,u}$). Contours of the EM-ETGM (b) growth rate and (c) real frequency. Large $\beta_{e,u}$ is found to be destabilizing, whereas small $\beta_{e,u}$ is found to be stabilizing.

relatively low $k_y \rho_s$ values. When β is very small, a similar trend emerges (not shown here), implying that the mode may be stable in the deep core region of low β plasmas. As shown in Fig. 9(b), modes have larger $k_y \rho_s$ in the deep core region, indicating a shorter wavelength nature of the mode. In Fig. 9(d), the value of $|\hat{A}_\parallel|^2$ is found to be large in the core and then decreases as $\hat{\rho}$ increases, indicating that the mode in the deep core region is electromagnetic.

J. Beta gradient

The β' scan was carried out by directly altering the value of β' in the model. Figure 10 demonstrates the dependence of β gradient (β')

on ETG modes for experimental β' and two times the experimental β' ($2\beta'$). The effect of β' through geometry on ETG modes is considered. The ETG mode real frequencies, corresponding $k_y \rho_s$, $|\hat{A}_\parallel|^2$ and average curvature ($\bar{G}$), are also plotted. Both the growth rate and the real frequency are found to be decreasing with increasing β'. The effect of β' is found to be more pronounced in the deep core region, where modes are more electromagnetic in character. The most unstable mode's $k_y \rho_s$ is also shown to be affected by β'. Increased β' decreases $|\hat{A}_\parallel|^2$, hence lowering the growth rate. Increased β' turns bad curvature to good curvature in the deep core area and hence decreases the growth rate. The change in magnetic perturbation, $k_y \rho_s$, and average curvature is found to be small in the edge region, implying that β'
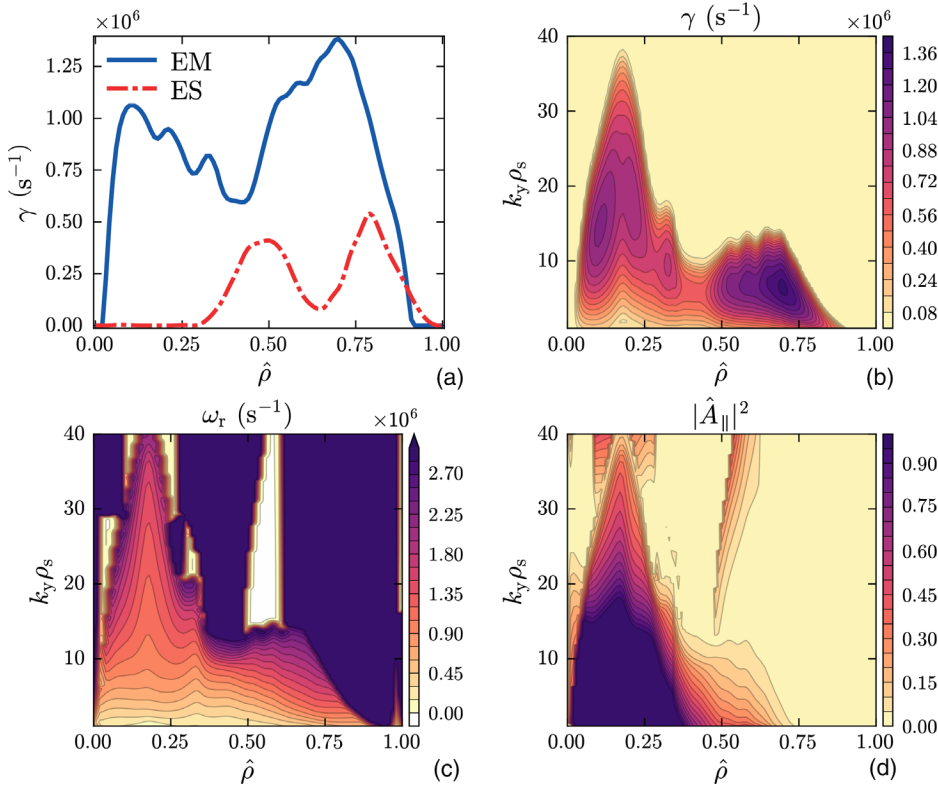
FIG. 9. (a) ETG modes with electromagnetic effects (EM) and without electromagnetic effects (ES, electrostatic). Contours of the EM-ETGM (b) growth rate and (c) real frequency and (d) $|\hat{A}_\parallel|^2$. The mode is found to be purely electromagnetic in the deep core.
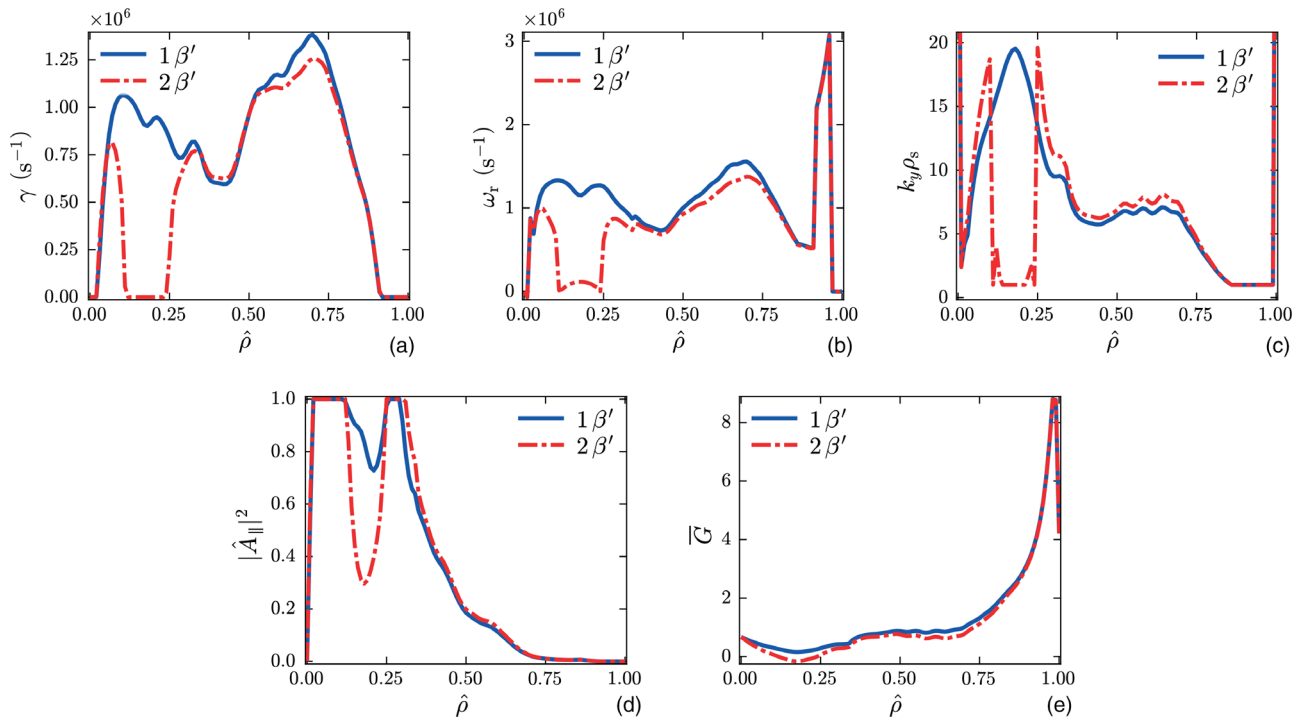
FIG. 10. (a) ETG mode growth rate, (b) real frequency, (c) $k_y \rho_s$, (d) $|\hat{A}_\parallel|^2$, and (e) average curvature ($\bar{G}$) for two different values of plasma β gradient, β'. The increase in β' has stabilizing effects on ETG modes.

stabilizing effects are also small there. Increasing β' stabilizes the mode by achieving a high density gradient through pellet injection. However, pellet injection is not available in the NSTX tokamak.

In summary of Subsections IV I and IV J, EM-ETGMs are electromagnetic in nature and have short wavelengths in the low shear and low $\hat{s}/q$ region in the deep core of the NSTX plasma. Near the edge, the modes have longer wavelengths and an increasingly electrostatic nature. Increasing β' changes bad curvature to good curvature in the deep core, reducing $|\hat{A}_\parallel|^2$ and the growth rate of the mode.

K. Isotope mass

An isotope mass comparison was conducted by setting the input values of mean atomic mass of the hydrogen ions to either 1, 2, or 3, and then by updating the mean atomic mass of thermal ions in accordance with these values. Additionally, a fixed value of $k_y \rho_s = 8$ was taken for all values of $\hat{\rho}$. Otherwise, no other input variables were changed. The isotopic mass dependence of hydrogen on the EM-ETGM growth rate, real frequency, and electron thermal diffusivity is displayed in Fig. 11.
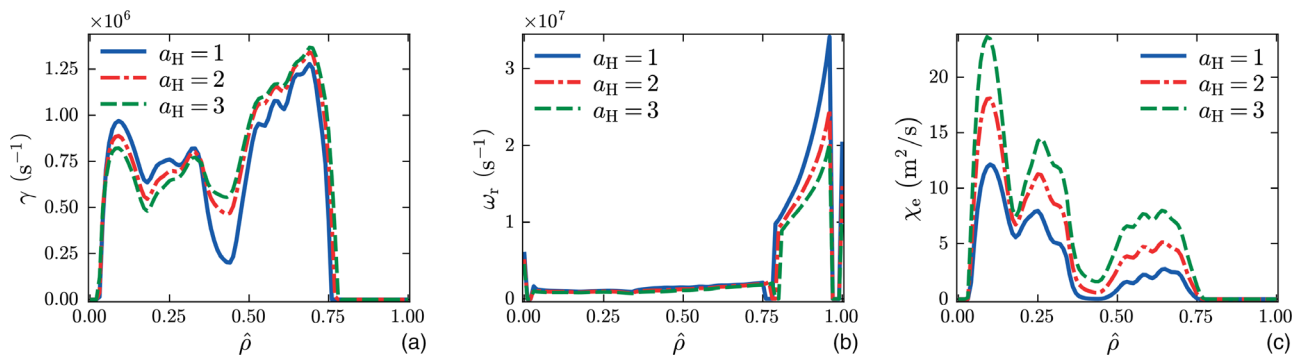
FIG. 11. EM-ETGM (a) growth rate, (b) real frequency, and (c) electron thermal diffusivity for three isotopes of hydrogen atom are plotted using a fixed $k_y \rho_s = 8$ for all radial points. The growth rate of the electromagnetic mode in the center decreases as the ion mass increases, whereas the growth rate of the mode in the confinement region slightly increases.
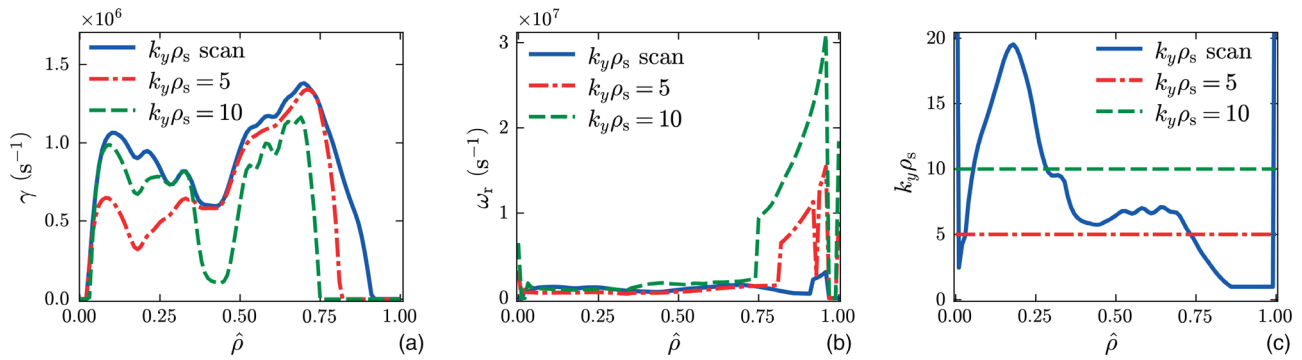
FIG. 12. (a) Fixed vs variable $k_y\rho_s$ scans influence ETG modes growth rate and (b) real frequency. (c) Fixed $k_y\rho_s$ values and $k_y\rho_s$ values associated with the most unstable mode found in the scan of $k_y\rho_s$. The $k_y\rho_s$ associated with the most unstable mode is observed to be decreasing at the plasma edge where the temperature gradient is increasing and the mode's electrostatic characteristic increases.

Numerous tokamak experiments have demonstrated that plasma confinement properties improve when increasing the atomic mass of the hydrogen isotope used (H, D, and T). In this study, the influence of ion mass on the mode growth rate using fixed $k_y\rho_s$ is found to be both stabilizing and destabilizing. As the ion mass grows, the growth rate of the electromagnetic Alfvén mode in the center decreases due to a decrease in Alfvén frequency, while the growth rate of the mode in the confinement region somewhat increases where the mode is more electrostatic than electromagnetic in nature. The ETG thermal diffusivity, on the other hand, increases with ion mass due to the dependence of diffusivity on ion mass, which negatively impacts confinement. The decrease in the poloidal wave number with increased ion mass causes diffusivity to increase. It is a theoretical gyro-Bohm trend. It is argued that stabilizing isotopic effects in experiments may be attributable to indirect effects, such as increased flow shear, Z-effective, and multi-scale physics, rather than direct isotopic effects.[44–46]

L. Fixed vs varied wavenumber

EM-ETGMs as a function of $\hat{\rho}$ with fixed and varied $k_y\rho_s$ are shown in Fig. 12. The modes are electromagnetic, toroidal, and short wavelength ($k_y\rho_s \leq 20$) in the region $\hat{\rho} < 0.5$, but the modes are nearly electrostatic and longer wavelength ($k_y\rho_s \leq 7.0$) in the region

$0.65 < \hat{\rho} < 0.85$, while the modes exhibit $k_y\rho_s \leq 1.0$ near $\hat{\rho} = 0.9$, indicating that ETG modes can exist in longer wavelength regime. Therefore, ETG modes with shorter, intermediate, and longer wavelengths are reported. The conventional ETG modes are generally electrostatic, and large β can stabilize these modes. The ETG modes reported in this study, on the other hand, are found to be unstable in almost all NSTX discharges considered, despite the fact that NSTX discharges are known to have large β values.

M. Flow shear

The EM-ETGM growth rate and real frequency as a function of $\hat{\rho}$ with and without flow shear are shown in Fig. 13. The effect of flow shear on ETG modes is found to be small. Growth rates of the ETG modes are found to be greater than the equilibrium flow shear.

Growth rate is found near the edge when the minimum $k_y\rho_s$ value is decreased from 1.0 to 0.1 during the scan. However, this instability is suppressed due to substantial values of flow shear toward the edge. The discovery of a low $k_y\rho_s$ ETG mode in the pedestal region agrees with gyrokinetic results.[47]

In the summary of Subsections IV K–IV M, the modes are electromagnetic, toroidal, short, intermediate, and long wavelength in different regions of the plasmas. The growth rate for purely electromagnetic modes decreases with increasing hydrogen isotopic
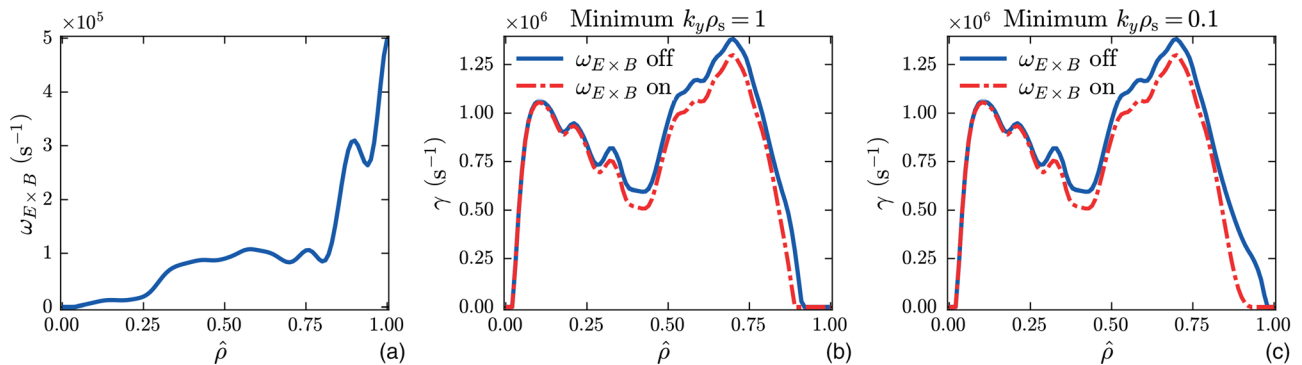
FIG. 13. (a) Equilibrium flow shear, (b) EM-ETGM growth rate with and without flow shear, and (c) EM-ETGM growth rate when the minimum $k_y\rho_s$ value used in the $k_y\rho_s$ scan is decreased from 1.0 to 0.1. The effect of flow shear on ETG modes is found to be small.
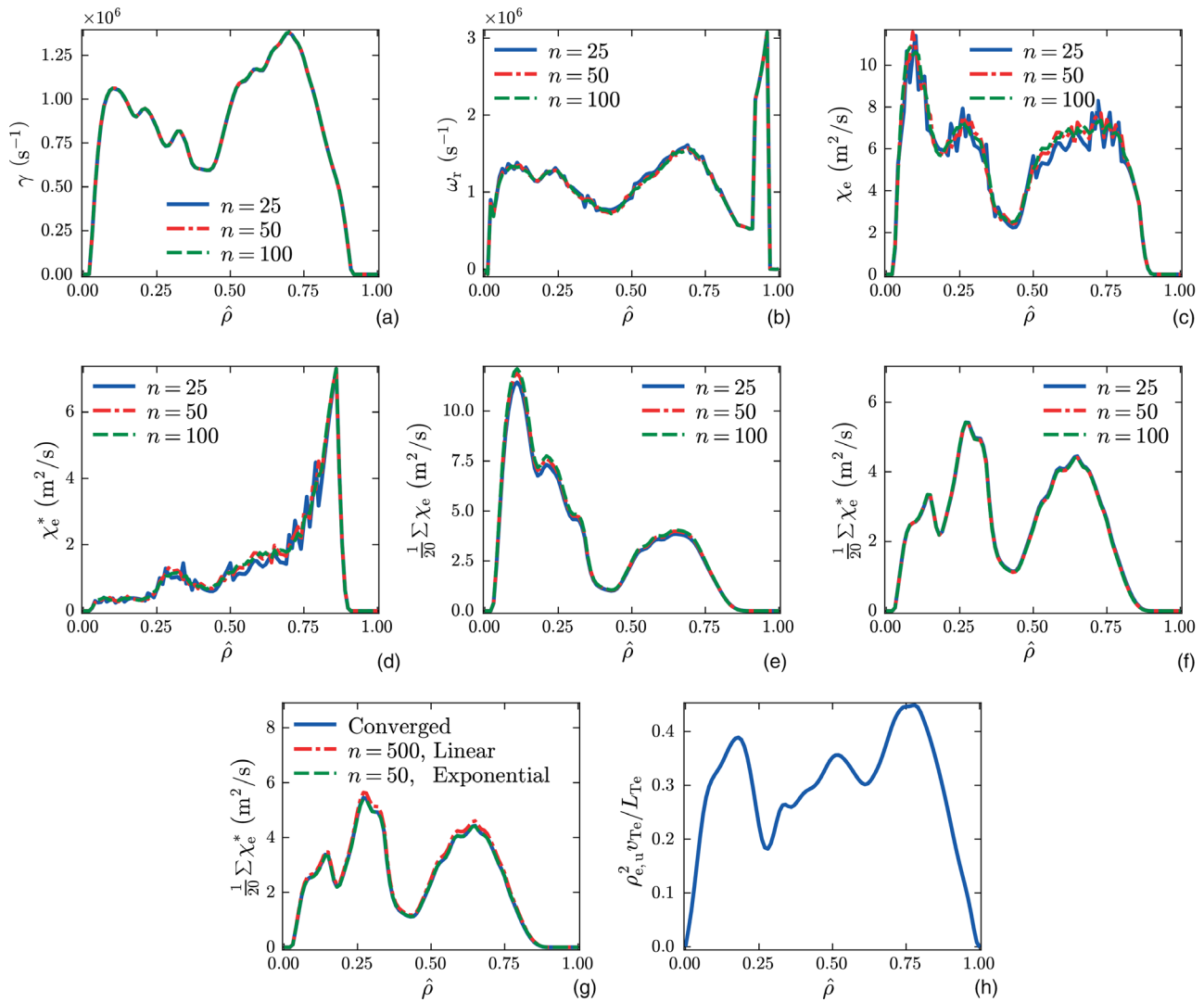
FIG. 14. (a) EM-ETGM growth rate and (b) real frequency vs $\hat{\rho}$ using $n = 25$, 50, and 100 k_y steps. Equations (21) and (22) are used to calculate electron thermal diffusivity using (c) and (d) the most unstable eigenmode and (e) and (f) the sum of all modes in the $k_y \rho_s$ spectrum at each $\hat{\rho}$, respectively. The diffusivity sums have been calibrated by a factor of $\frac{1}{20}$. (g) Electron diffusivity as a function of $\hat{\rho}$ using linear and exponential k_y increments. The converged line corresponds to one million linear k_y steps. The convergence rate of the k_y scan can be greatly improved when the shape of the k_y increments is matched with the rate that subsequent modes are changing. (h) gyroBohm diffusivity $\rho_e^2 v_{Te}/L_{Te}$ as a function of $\hat{\rho}$ is found to be substantially less than the EM-ETGM electron thermal diffusivity.

mass, whereas the growth rate for mixed modes (modes with magnetostatic and electrostatic characteristics) is only weakly affected. The $k_y \rho_s$ associated with the most unstable mode is observed to be decreasing at the plasma edge where the temperature gradient is increasing and the mode's electrostatic characteristic increases. The effect of flow shear on the mode growth rate is found to be small, except at the edge region where the mode growth rate is low and the flow shear is high.

N. Convergence of modes

Convergence studies are carried out in Fig. 14 to determine the required k_y step count (n). The EM-ETGM growth rate, real frequency, and electron thermal diffusivities [Eqs. (21) and (22)] are shown for $n = 25$, 50, and 100 k_y steps using different methods. Excellent convergence was found using $n = 100$ k_y steps for the most unstable mode. In practice, only $n = 50$ steps should yield satisfactory results. Fewer k_y steps are needed when summing modes in the electron thermal diffusivity, as only a majority of the largest modes need to be accounted for when obtaining the convergence of the sum over all k_y modes.

Convergence is also investigated by comparing k_y scans with linear and exponential k_y increments in Fig. 14(g). Exponential k_y increments are found to converge much faster than linear k_y increments. This is because exponential k_y increments are small (high-precision)

when the change in diffusivity between subsequent modes is large, and k_y increments are large (low-precision) when the change in diffusivity between subsequent modes is small.

In Fig. 14(h), the gyroBohm diffusivity $\rho_e^2 v_{Te}/L_{Te}$ as a function of $\hat{\rho}$ is displayed. The ETG thermal diffusivity is found to be much larger than the gyroBohm diffusivity, indicating that mixing length estimates based on the isomorphism between ETG and ITG are underestimated. It is worth noting that the diffusivity predicted using the most unstable modes is roughly ten times that of the gyroBohm diffusivity, a scale that matches the experimental thermal diffusivity determined by power balance analysis.[15,48] The sum of all the modes, on the other hand, yields a diffusivity that is substantially larger than the experimental thermal diffusivity.

O. Time and space dependence

Figure 15 depicts contour plots of the EM-ETGM growth rate (γ), real frequency (ω_r), drift frequency (ω_{*e}), magnetic drift frequency (ω_{De}), temperature gradient frequency (ω_{Te}), Alfvén frequency (ω_A), electron beta ($\beta_{e,u}$), vector potential ($|\hat{A}_\parallel|^2$), and scalar potential ($|\hat{\phi}|^2$) as a function of $\hat{\rho}$ and time for low collisionality NSTX discharge 138 536. The mode is found to be unstable even for small temperature gradient values in the low shear ($\hat{s}$) and low $\hat{s}/q$ deep core for a sufficiently large $\beta_{e,u}$. Transport due to ETG modes is discovered in the core region, where modes have more electromagnetic characteristics, as evidenced by high values of electromagnetic potential. The mode is more electrostatic in nature toward the edge region where electrostatic potential is large and beta is small. The Alfvén frequency is comparable
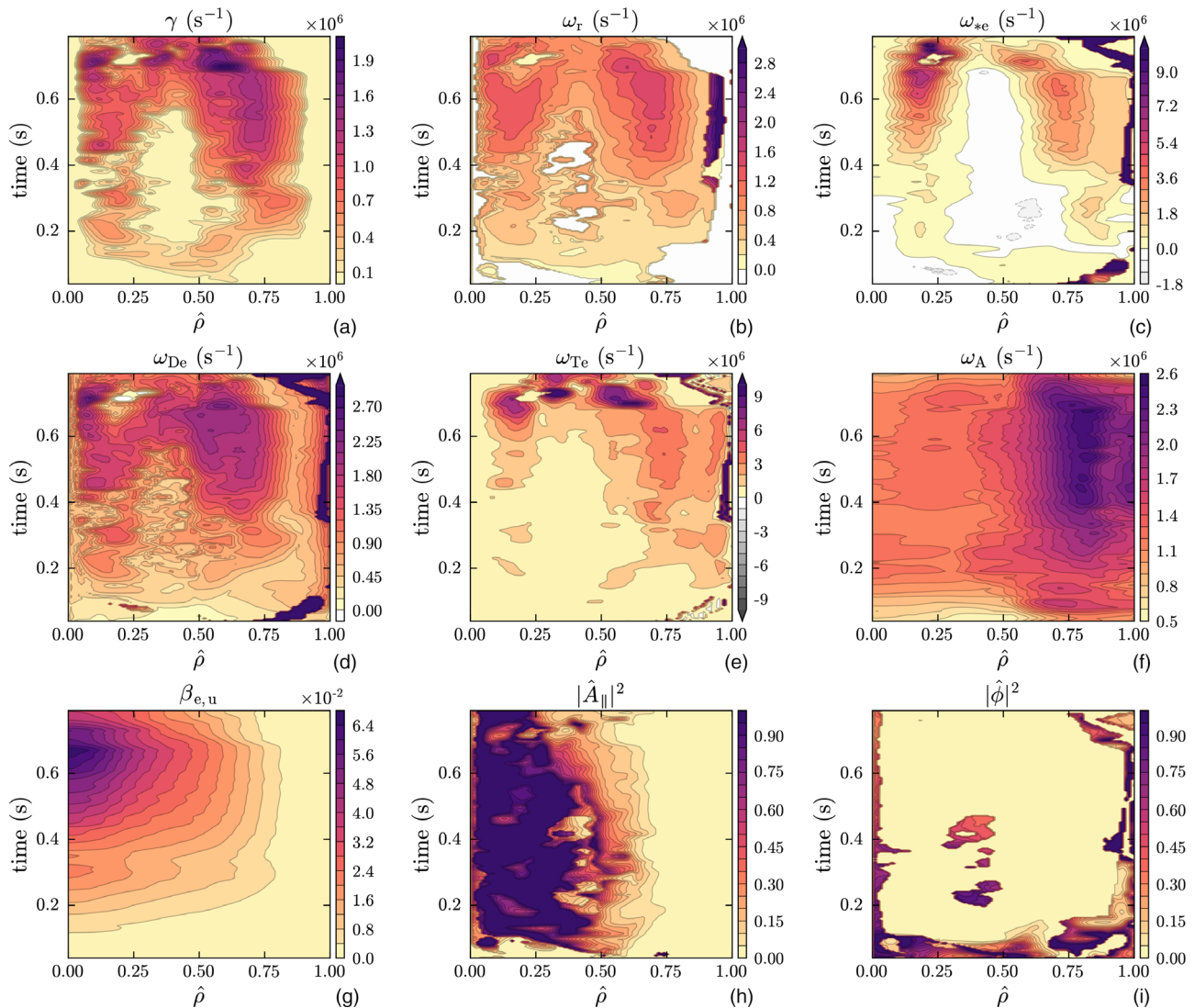
FIG. 15. Contour plots of the EM-ETGM (a) growth rate, (b) real frequency, and (c) drift frequency (ω_{*e}), (d) magnetic drift frequency (ω_{De}), (e) temperature gradient frequency (ω_{Te}), (f) Alfvén frequency (ω_A), (g) electron beta ($\beta_{e,u}$), (h) vector potential ($|\hat{A}_\parallel|^2$), and (i) scalar potential ($|\hat{\phi}|^2$) as a function of $\hat{\rho}$ and time for low collisionality NSTX discharge 138 536.

to the real frequency in the deep core, which indicates magnetic fluctuations are due to short wavelength Alfvén modes. It is worth noting that the modes naturally transition from electromagnetic characteristics in the deep core to electrostatic characteristics near the edge. Temperature gradients and curvature are found to be more responsive to modes than the density gradients or the plasma parameter η_e. Modes are discovered to resonate with ω_{De} and to have a faster growth rate when the electron temperature gradient drive is strong. Modes are found to be stable in the region where the direction of frequency is opposite the direction of diamagnetic drift frequency. Modes are also found to be stable where the magnetic drift frequency is much greater than the frequency of the modes. the EM-ETGM instability is strong because the magnitude and behavior of frequency and growth rate are similar.

Figure 16 depicts that the thermal diffusivity associated with EM-ETGM is computed in four different ways. These results show that all four methods produce similar results, with the exception of using the most unstable mode in the alternate diffusivity formula [Eq. (22)] as seen in Fig. 16(c), where the diffusivity in the core region almost disappears. These diffusivities will be tested for their ability to predict the electron temperature profile against various types of discharges for various tokamaks. It is planned that the EM-ETGM diffusivity will also be compared to the nonlinear CGYRO diffusivity, and if necessary, the EM-ETGM diffusivity will be calibrated.

V. SUMMARY AND DISCUSSION

A new model for electromagnetic electron temperature gradient modes (EM-ETGMs) is developed for tokamak plasmas. This model is

based on two-fluid equations that govern the dynamics of low-frequency, short-, intermediate-, and long-wavelength electromagnetic toroidal ETG driven drift modes. The model includes the effects of density, temperature, and magnetic field perturbation and gradients, electron inertia, curvature, collisionality, non-adiabatic ions, density dilution, Shafranov shift, gradient of β (β'), magnetic drift resonances and drift reversal, low and reverse magnetic shear, and flow shear. The gradients of electron temperature and density, magnetic-q, magnetic shear, electron temperature, electron density, magnetic field strength, electron β, β', isotopic effects, and collisionality are scanned to determine the dependency of the EM-ETGM real frequency, growth rate, and diffusivity. Convergence studies are also performed to determine the number of unstable modes required in the k_y spectrum at each radial location.

Conventional ETG modes are short wavelength with adiabatic ions. However, non-adiabatic ion effects, including $\mathbf{E} \times \mathbf{B}$ and polarization drifts, are taken into account without including ion-temperature-gradient mode fluctuations in the new EM-ETGM. The EM-ETGM frequency is comparable to both the ion magnetic and electron drift frequencies ensuring that the ion dynamic does not become adiabatic. These non-adiabatic effects may provide stabilizing effects to the ETG modes even before drift reversal occurs. The conventional ETG modes have frequency of the order of $\omega \gg k_\parallel v_{Te}$, whereas EM-ETGM has frequencies of the order of $\omega \le k_\parallel v_{Te}$.

Furthermore, conventional ETG modes are generally electrostatic and large β may stabilize these modes. On the other hand, the EM-ETGM reported in this study are found to be unstable in almost all
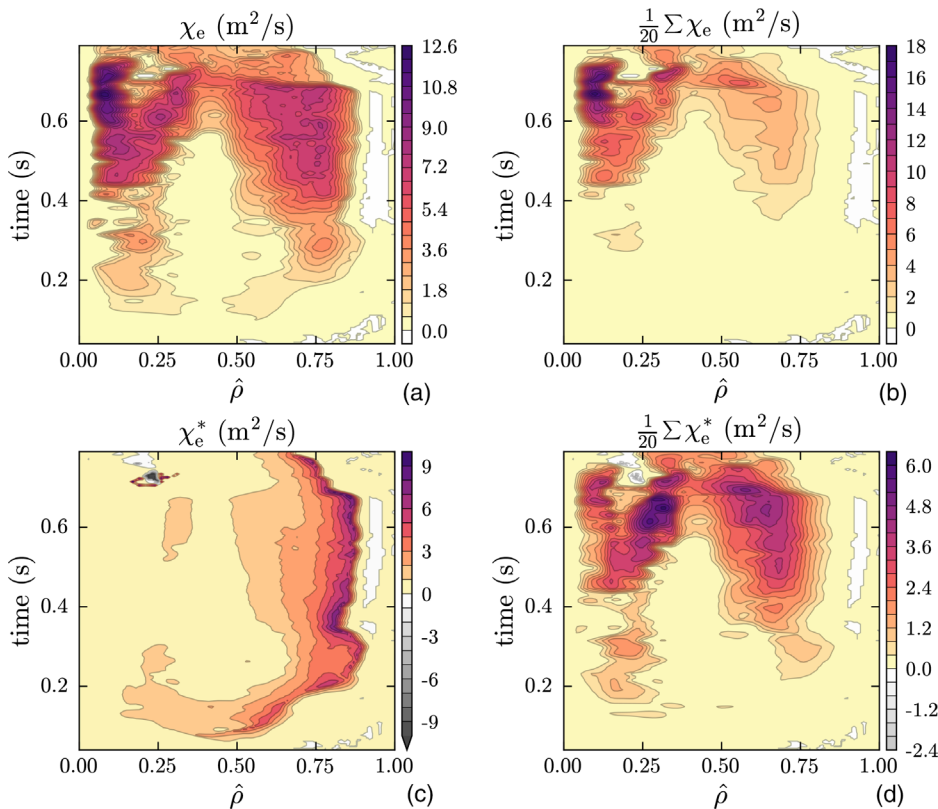
FIG. 16. Contour plots of the EM-ETGM diffusivity (a) using eigenvectors associated with the most unstable mode at each $\hat{\rho}$ in Eq. (21), (b) summing over eigenvectors associated with the $k_y \rho_s$ spectrum at each $\hat{\rho}$, (c) using the most unstable mode growth rate in the alternate diffusivity formula in Eq. (22), and (d) summing over growth rates associated with the $k_y \rho_s$ spectrum in the alternate diffusivity formula. The diffusivity sums have been calibrated by a factor of $\frac{1}{20}$.

NSTX discharges considered, despite the fact that NSTX discharges are known to have large β values. The electromagnetic ETG mode is found to be a toroidal version of the drift Alfvén mode, which becomes unstable due to charge separation caused by an unfavorable magnetic field gradient and curvature electron drift in the presence of an electron temperature and density gradient. This shows that magnetic fluctuations due to short wavelength Alfvén modes in the core region of the NSTX discharges cause turbulence and anomalous electron thermal transport.

In our EM-ETGM modeling, the fastest-growing linear ETG mode is assumed to have a small radial wavenumber, resulting in a smaller total finite Larmor radius. As a result, ETG streamers can be obtained linearly. Nonlinearly, this streamer is then assumed to be torn apart by flow shear. The transport from ETG modes is obtained using eigenvectors associated with the most unstable mode and their sidebands in the ETG spectrum at each radial location. The electron temperature gradient and curvature are found to be more responsive to modes than the absolute density gradients or the plasma parameter η_e. Overall, these modes are curvature and electron temperature gradient driven. However, the increase in density gradient caused by pellet injection can be seen in tokamak experiments and can be used as a knob to stabilize these modes. However, pellet injection is not available in the NSTX tokamak.

In addition, the mode is found to be substantially destabilized when q is increased and stabilized for large values of B_u, indicating that modes will be less destabilized in NSTX-U discharges due to large values of B_u. The mode is found to be stabilized with increasing β'. The effects of reverse magnetic shear are found to be ETG mode stabilizing, resulting in the suppression of electron thermal transport, which is responsible for the ITB region in the electron temperature profile of NSTX discharges. Drift reversal occurs when temperature and density gradients, q, T_e, n_e, and $\beta_{e,u}$ are increased significantly. The effects of various $k_\parallel$ estimations, turning on and off collisions, magnetic shear vs effective shear, flow shear, and isotope mass on the EM-ETGM growth rates are not significant. The electron thermal diffusivity associated with EM-ETGM is calculated using different methods. The diffusivity is discovered to be much greater than the gyroBohm estimate. The diffusivity calculated using the most unstable ETG modes is found to be on a scale consistent with the experimental diffusivity determined by power balance analysis.

Several previously reported gyrokinetic results are reproduced, including the stabilizing effects of steep density gradients, reverse magnetic shear, large $\beta_{e,u}$ and β', large collisionality (n_e scan), destabilizing effects of q, and stabilizing and destabilizing effects of toroidicity. The EM-ETGM diffusivity will be compared to the nonlinear CGYRO diffusivity, and the EM-ETGM diffusivity will be calibrated if necessary. The EM-ETGM model will be used as a component of the multimode anomalous transport module in the predictive integrated modeling code TRANSP to predict time-dependent electron temperature profile in tokamak plasmas.

ACKNOWLEDGMENTS

AUTHOR DECLARATIONS
Conflict of Interest

The authors have no conflicts to disclose.

Author Contributions

Tariq Rafiq: Writing – original draft (lead); Writing – review & editing (lead). **Chris Wilson:** Writing – review & editing (supporting). **L Luo:** Writing – review & editing (supporting). **Jan Weiland:** Writing – review & editing (supporting). **Eugenio Schuster:** Writing – review & editing (supporting). **Alexei Y Pankin:** Writing – review & editing (supporting). **Walter Guttenfelder:** Writing – review & editing (supporting). **Stanley M. Kaye:** Writing – review & editing (supporting).

DATA AVAILABILITY

The digital data for this paper can be found at the Princeton Plasma Physics Laboratory http://arks.princeton.edu/ark:/88435/dsp015d86p342b [DataSpace].

REFERENCES

[1] W. Guttenfelder, D. Battaglia, E. Belova, N. Bertelli, M. Boyer, C. Chang, A. Diallo, V. Duarte, F. Ebrahimi, E. Emdee, N. Ferraro, E. Fredrickson, N. Gorelenkov, W. Heidbrink, Z. Ilhan, S. Kaye, E.-H. Kim, A. Kleiner, F. Laggner, M. Lampert, J. Lestz, C. Liu, D. Liu, T. Looby, N. Mandell, R. Maingi, J. Myra, S. Munaretto, M. Podestà, T. Rafiq, R. Raman, M. Reinke, Y. Ren, J. R. Ruiz, F. Scotti, S. Shiraiwa, V. Soukhanovskii, P. Vail, Z. Wang, W. Wehner, A. White, R. White, B. Woods, J. Yang, S. Zweben, S. Banerjee, R. Barchfeld, R. Bell, J. Berkery, A. Bhattacharjee, A. Bierwage, G. Canal, X. Chen, C. Clauser, N. Crocker, C. Domier, T. Evans, M. Francisquez, K. Gan, S. Gerhardt, R. Goldston, T. Gray, A. Hakim, G. Hammett, S. Jardin, R. Kaita, B. Koel, E. Kolemen, S.-H. Ku, S. Kubota, B. LeBlanc, F. Levinton, J. Lore, N. Luhmann, R. Lunsford, R. Maqueda, J. Menard, J. Nichols, M. Ono, J.-K. Park, F. Poli, T. Rhodes, J. Riquezes, D. Russell, S. Sabbagh, E. Schuster, D. Smith, D. Stotler, B. Stratton, K. Tritz, W. Wang, and B. Wirth, "NSTX-u theory, modeling and analysis results," Nucl. Fusion **62**, 042023 (2022).

[2] Y. C. Lee, J. Q. Dong, P. N. Guzdar, and C. S. Liu, "Collisionless electron temperature gradient instability," Phys. Fluids **30**, 1331–1339 (1987).

[3] W. Horton, B. G. Hong, and W. M. Tang, "Toroidal electron temperature gradient driven drift modes," Phys. Fluids **31**, 2971–2983 (1988).

[4] A. M. Mirza, T. Rafiq, A. Qamar, G. Murtaza, R. T. Faria, and P. K. Shukla, "Anomalous heat transport and vortex formation due to electron–temperature–gradient driven drift waves in a sheared flow plasma," Phys. Scr. **60**, 261–264 (1999).

[5] W. Dorland, F. Jenko, M. Kotschenreuther, and B. N. Rogers, "Electron temperature gradient turbulence," Phys. Rev. Lett. **85**, 5579–5582 (2000).

[6] F. Jenko, W. Dorland, and G. W. Hammett, "Critical gradient formula for toroidal electron temperature gradient modes," Phys. Plasmas **8**, 4096–4104 (2001).

[7] R. Singh, V. Tangri, H. Nordman, and J. Weiland, "Fluid description of electron temperature gradient driven drift modes," Phys. Plasmas **8**, 4340–4350 (2001).

[8] A. Hirose and M. Elia, "Short wavelength temperature gradient driven modes in tokamaks. II. electron mode," Phys. Plasmas **9**, 4664–4670 (2002).

[9] T. Davydova, G. Bateman, A. H. Kritz, and A. Pankin, "Toroidal electron temperature gradient mode structure in the presence of nonuniform background flows," Phys. Plasmas **10**, 3614–3628 (2003).

[10] A. Hirose, "Effects of charge non-neutrality and finite β on the electron temperature gradient mode," Phys. Plasmas **10**, 4567–4569 (2003).

[11] W. Horton, B. Hu, J. Q. Dong, and P. Zhu, "Turbulent electron thermal transport in tokamaks," New J. Phys. **5**, 14 (2003).

[12] C. Bourdelle, W. Dorland, X. Garbet, G. W. Hammett, M. Kotschenreuther, G. Rewoldt, and E. J. Synakowski, "Stabilizing impact of high gradient of β on microturbulence," Phys. Plasmas **10**, 2881–2887 (2003).

[13]S. M. Kaye, R. E. Bell, D. Gates, B. P. LeBlanc, F. M. Levinton, J. E. Menard, D. Mueller, G. Rewoldt, S. A. Sabbagh, W. Wang, and H. Yuh, "Scaling of electron and ion transport in the high-power spherical torus NSTX," Phys. Rev. Lett. **98**, 175002 (2007).

[14]W. Guttenfelder, J. Peterson, J. Candy, S. Kaye, Y. Ren, R. Bell, G. Hammett, B. LeBlanc, D. Mikkelsen, W. Nevins, and H. Yuh, "Progress in simulating turbulent electron thermal transport in NSTX," Nucl. Fusion **53**, 093022 (2013).

[15]Y. Ren, E. Belova, N. Gorelenkov, W. Guttenfelder, S. Kaye, E. Mazzucato, J. Peterson, D. Smith, D. Stutman, K. Tritz, W. Wang, H. Yuh, R. Bell, C. Domier, and B. LeBlanc, "Recent progress in understanding electron thermal transport in NSTX," Nucl. Fusion **57**, 072002 (2017).

[16]J. Zielinski, A. I. Smolyakov, P. Beyer, and S. Benkadda, "Electromagnetic electron temperature gradient driven instability in toroidal plasmas," Phys. Plasmas **24**, 024501 (2017).

[17]J. F. Parisi, F. I. Parra, C. M. Roach, C. Giroud, W. Dorland, D. R. Hatch, M. Barnes, J. C. Hillesheim, N. Aiba, J. Ball, P. G. Ivanov, and J. contributors, "Toroidal and slab ETG instability dominance in the linear spectrum of JET-ILW pedestals," Nucl. Fusion **60**, 126045 (2020).

[18]S. Maeyama, S. Kusaka, and T. H. Watanabe, "Effects of ion polarization and finite β on heat transport in slab electron temperature gradient driven turbulence," Phys. Plasmas **28**, 052512 (2021).

[19]W. Guttenfelder and J. Candy, "Resolving electron scale turbulence in spherical tokamaks with flow shear," Phys. Plasmas **18**, 022506 (2011).

[20]F. Jenko, W. Dorland, M. Kotschenreuther, and B. N. Rogers, "Electron temperature gradient driven turbulence," Phys. Plasmas **7**, 1904–1910 (2000).

[21]T. Fujita, S. Ide, H. Shirai, M. Kikuchi, O. Naito, Y. Koide, S. Takeji, H. Kubo, and S. Ishida, "Internal transport barrier for electrons in JT-60U reversed shear discharges," Phys. Rev. Lett. **78**, 2377–2380 (1997).

[22]A. Hubbard, S.-G. Baek, D. Brunner, A. Creely, I. Cziegler, E. Edlund, J. Hughes, B. LaBombard, Y. Lin, Z. Liu, E. Marmar, M. Reinke, J. Rice, B. Sorbom, C. Sung, J. Terry, C. Theiler, E. Tolman, J. Walk, A. White, D. Whyte, S. Wolfe, and X. X. Wukitch, "Physics and performance of the i-mode regime over an expanded operating space on Alcator C-mod," Nucl. Fusion **57**, 126039 (2017).

[23]D. R. Smith, S. M. Kaye, W. Lee, E. Mazzucato, H. K. Park, R. E. Bell, C. W. Domier, B. P. LeBlanc, F. M. Levinton, N. C. Luhmann, J. E. Menard, and H. Yuh, "Observations of reduced electron gyroscale fluctuations in national spherical torus experiment h-mode plasmas with large $e \times b$ flow shear," Phys. Rev. Lett. **102**, 225005 (2009).

[24]Y. Ren, S. M. Kaye, E. Mazzucato, W. Guttenfelder, R. E. Bell, C. W. Domier, B. P. LeBlanc, K. C. Lee, N. C. Luhmann, D. R. Smith, and H. Yuh, "Density gradient stabilization of electron temperature gradient driven turbulence in a spherical tokamak," Phys. Rev. Lett. **106**, 165005 (2011).

[25]T. Rafiq, A. H. Kritz, J. Weiland, A. Y. Pankin, and L. Luo, "Physics basis of multi-mode anomalous transport module," Phys. Plasmas **20**, 032506 (2013).

[26]T. Rafiq, S. Kaye, W. Guttenfelder, J. Weiland, E. Schuster, J. Anderson, and L. Luo, "Microtearing instabilities and electron thermal transport in low and high collisionality NSTX discharges," Phys. Plasmas **28**, 022504 (2021).

[27]J. Weiland and A. Zagorodny, "Drift wave theory for transport in tokamaks," Rev. Mod. Plasma Phys. **3**, 8 (2019).

[28]J. Weiland, A. Zagorodny, and T. Rafiq, "Theory for transport in magnetized plasmas," Phys. Scr. **95**, 105607 (2020).

[29]R. E. Waltz and R. L. Miller, "Ion temperature gradient turbulence simulations and plasma flux surface shape," Phys. Plasmas **6**, 4265–4271 (1999).

[30]D. D. Hua, X. Q. Xu, and T. K. Fowler, "Ion temperature gradient modes in noncircular tokamak geometry," Phys. Fluids B **4**, 3216–3225 (1992).

[31]J. W. Connor and O. P. Pogutse, "On the relationship between mixing length and strong turbulence estimates for transport due to drift turbulence," Plasma Phys. Controlled Fusion **43**, 155–175 (2001).

[32]J. Weiland and H. Nordman, "Enhanced confinement regimes in transport code simulations of toroidal drift wave transport," Nucl. Fusion **31**, 390–394 (1991).

[33]H. Nordman and J. Weiland, "Transport due to toroidal η_i mode turbulence in tokamaks," Nucl. Fusion **29**, 251–263 (1989).

[34]J. Weiland, *Stability and Transport in Magnetic Confinement Systems* (Springer, New York, Heidelberg, 2012).

[35]F. Jenko and W. Dorland, "Prediction of significant tokamak turbulence at electron gyroradius scales," Phys. Rev. Lett. **89**, 225001 (2022).

[36]L. Luo, T. Rafiq, and A. Kritz, "Improved multi-mode anomalous transport module for tokamak plasmas," Comput. Phys. Commun. **184**, 2267–2276 (2013).

[37]A. Hirose and N. Joiner, "Short wavelength ballooning mode in tokamaks," in *New Aspects of Plasma Physics* (World Scientific, 2008), p. 476.

[38]M. Greenwald, D. Gwinn, S. Milora, J. Parker, R. Parker, S. Wolfe, M. Besen, F. Camacho, S. Fairfax, C. Fiore, M. Foord, R. Gandy, C. Gomez, R. Granetz, B. LaBombard, B. Lipschultz, B. Lloyd, E. Marmar, S. McCool, D. Pappas, R. Petrasso, P. Pribyl, J. Rice, D. Schuresko, Y. Takase, J. Terry, and R. Watterson, "Energy confinement of high-density pellet-fueled plasmas in the Alcator C tokamak," Phys. Rev. Lett. **53**, 352–355 (1984).

[39]J. R. Ruiz, Y. Ren, W. Guttenfelder, A. E. White, S. M. Kaye, B. P. Leblanc, E. Mazzucato, K. C. Lee, C. W. Domier, D. R. Smith, and H. Yuh, "Stabilization of electron-scale turbulence by electron density gradient in national spherical torus experiment," Phys. Plasmas **22**, 122501 (2015).

[40]J. L. Peterson, R. Bell, J. Candy, W. Guttenfelder, G. W. Hammett, S. M. Kaye, B. LeBlanc, D. R. Mikkelsen, D. R. Smith, and H. Y. Yuh, "Suppressing electron turbulence and triggering internal transport barriers with reversed magnetic shear in the national spherical torus experiment," Phys. Plasmas **19**, 056120 (2012).

[41]J. Connor, T. Fukuda, X. Garbet, C. Gormezano, V. Mukhovatov, and M. Wakatani, the ITB Database Group, the ITPA Topical Group on Transport, and Internal Barrier Physics, "A review of internal transport barrier physics for steady-state operation of tokamaks," Nucl. Fusion **44**, R1–R49 (2004).

[42]H. Y. Yuh, F. M. Levinton, R. E. Bell, J. C. Hosea, S. M. Kaye, B. P. LeBlanc, E. Mazzucato, J. L. Peterson, D. R. Smith, J. Candy, R. E. Waltz, C. W. Domier, N. C. Luhmann, W. Lee, and H. K. Park, "Internal transport barriers in the national spherical torus experiment," Phys. Plasmas **16**, 056120 (2009).

[43]H. Y. Yuh, S. M. Kaye, F. M. Levinton, E. Mazzucato, D. R. Mikkelsen, D. R. Smith, R. E. Bell, J. C. Hosea, B. P. LeBlanc, J. L. Peterson, H. K. Park, and W. Lee, "Suppression of electron temperature gradient turbulence via negative magnetic shear in NSTX," Phys. Rev. Lett. **106**, 055003 (2011).

[44]T. Hahm, L. Wang, W. Wang, E. Yoon, and F. Duthoit, "Isotopic dependence of residual zonal flows," Nucl. Fusion **53**, 072002 (2013).

[45]Y. Xu, C. Hidalgo, I. Shesterikov, A. Krämer-Flecken, S. Zoletnik, M. Van Schoor, M. Vergote, and T. T. the, "Isotope effect and multiscale physics in fusion plasmas," Phys. Rev. Lett. **110**, 265005 (2013).

[46]A. Bustos, A. Bañón Navarro, T. Görler, F. Jenko, and C. Hidalgo, "Microturbulence study of the isotope effect," Phys. Plasmas **22**, 012305 (2015).

[47]D. Told, F. Jenko, P. Xanthopoulos, L. D. Horton, and E. Wolfrum, "Gyrokinetic microinstabilities in ASDEX upgrade edge plasmas," Phys. Plasmas **15**, 102306 (2008).

[48]Y. Ren, W. Guttenfelder, S. M. Kaye, E. Mazzucato, R. E. Bell, A. Diallo, C. W. Domier, B. P. LeBlanc, K. C. Lee, D. R. Smith, and H. Yuh, "Experimental study of parametric dependence of electron scale turbulence in a spherical tokamak," Phys. Plasmas **19**, 056125 (2012).